

JAYCOR SAN DIEGO CA

F/O 20/3

ANALYTICAL INVESTIGATION OF EMITTING PROBES IN AN IONIZED PLASMA--ETC(U)

APR 81 R E LEADON, A J WOODS, E P WENAAS

F19628-79-C-0121

JAYCOR-J200-80-250A/2172

AFGL-TR-81-0138

NL

1 of 1
N:
2024-166

END
DATE
FILMED
10-81
DTIC

LEVEL *77*

12 *92*

AFGL-TR-81-0138

AD A104166

**ANALYTICAL INVESTIGATION OF EMITTING
PROBES IN AN IONIZED PLASMA**

R. E. Leadon
A. J. Woods
E. P. Wenaas
H. H. Klein

JAYCOR
11011 Torreyana Road
P.O. Box 85154
San Diego, California 92138

Final Report
July 1979 to July 1980

April 12, 1981

Approved for public release; distribution unlimited

AIR FORCE GEOPHYSICS LABORATORY
AIR FORCE SYSTEMS COMMAND
UNITED STATES AIR FORCE
HANSCOM AFB, MASSACHUSETTS 01731

DTIC
ELECTE
SEP 14 1981
S **D**
H

DTIC FILE COPY

81 9 14 069

Qualified requestors may obtain additional copies from the
Defense Technical Information Center. All others should
apply to the National Technical Information Service.

UNCLASSIFIED

SECURITY CLASSIFICATION OF THIS PAGE (When Data Entered)

REPORT DOCUMENTATION PAGE		READ INSTRUCTIONS BEFORE COMPLETING FORM
1. REPORT NUMBER AFGL-TR-81-0138	2. GOVT ACCESSION NO. AD-A104 166	3. RECIPIENT'S CATALOG NUMBER
4. TITLE (and Subtitle) ANALYTICAL INVESTIGATION OF EMITTING PROBES IN AN IONIZED PLASMA		5. TYPE OF REPORT & PERIOD COVERED Final Report. July 1979 to July 1980
7. AUTHOR(s) R. E./Leadon, A. J./Woods, E. P./Wenaas, H. H./Klein		6. PERFORMING ORG. REPORT NUMBER J200-80-250A/2172
9. PERFORMING ORGANIZATION NAME AND ADDRESS JAYCOR 11011 Torreyana Road, P.O. Box 85154 San Diego, CA 92138		8. CONTRACT OR GRANT NUMBER F19628-79-C-0121
11. CONTROLLING OFFICE NAME AND ADDRESS Air Force Geophysics Laboratory Hanscom AFB, Massachusetts 01731 Monitor/Charles Dubs/PHI		10. PROGRAM ELEMENT, PROJECT, TASK AREA & WORK UNIT NUMBERS 62101F 760115AA
14. MONITORING AGENCY NAME & ADDRESS (if different from Controlling Office)		12. REPORT DATE April 12, 1981
		13. NUMBER OF PAGES 77
		15. SECURITY CLASS (of this report) Unclassified
		15a. DECLASSIFICATION DOWNGRADING SCHEDULE
16. DISTRIBUTION STATEMENT (of this Report) Approved for public release; distribution unlimited		
17. DISTRIBUTION STATEMENT (of the abstract entered in Block 20, if different from Report)		
18. SUPPLEMENTARY NOTES		
19. KEY WORDS (Continue on reverse side if necessary and identify by block number) atmospheric probes, charged-particle beams, plasma effects, probe potentials, ionization effects, geomagnetic effects, computer simulation		
20. ABSTRACT (Continue on reverse side if necessary and identify by block number) Analytical and computer-model studies have been made of the electrostatic potentials achieved by electron- and ion-emitting atmospheric probes. The variables that were considered include the beam species, their energy and current, the density and temperature of the ambient plasma, ionization of the neutral atmosphere by the plasma electrons which supply the replacement current for electron-emitting probes, and the effects of the geomagnetic field on trajectories of the charged particles. Mean ionization distances as large		

DTIC
SELECTED
SEP 14 1981
H

DD FORM 1473 EDITION OF 1 NOV 65 IS OBSOLETE

UNCLASSIFIED

SECURITY CLASSIFICATION OF THIS PAGE (When Data Entered)

UNCLASSIFIED

SECURITY CLASSIFICATION OF THIS PAGE(When Data Entered)

ABSTRACT (Continued)

as 100 meters have a pronounced effect on the potentials of electron-emitting probes for beam currents greater than 0.01 amperes. The calculations indicate a peak in the I-V curve for such probes.

Accession For	
NTIS GRA&I	<input checked="checked" type="checkbox"/>
DTIC TAB	<input type="checkbox"/>
Unannounced	<input type="checkbox"/>
Justification	
By	
Distribution/	
Availability Codes	
Avail and/or	
Dist	Special
A	

UNCLASSIFIED

SECURITY CLASSIFICATION OF THIS PAGE(When Data Entered)

TABLE OF CONTENTS

ABSTRACT	1
1. INTRODUCTION	3
1.1 Background.....	3
1.2 Approach	4
1.3 Report Organization.....	7
2. ENVIRONMENTS AND DATA FOR IONOSPHERIC PROBE EXPERIMENTS.....	8
3. SPHERICALLY SYMMETRIC STEADY-STATE MODEL	13
3.1 Lam's Model.....	13
3.2 Series Solution in Sheath Region.....	15
3.3 Analytical Results.....	17
3.4 Computer Model and Results.....	25
3.4.1 Model Without Ionization.....	25
3.4.2 Model with Ionization.....	28
3.5 Orbital Limiting	35
4. ABORC CALCULATIONS	37
4.1 Description of the Standard ABORC Code	38
4.2 Modifications for the Plasma-Probe Calculation	38
4.3 Computer Model for the Probe, Beam, and Plasma	42
4.4 Calculated Behavior of the Probe for Simple Conditions	45
4.5 Effects of the Geomagnetic Field	46
4.6 Effects of Ionization of Neutrals on Early-Time Behavior	50
4.7 Suggested Experimental Measurements Based on Calculated Early-Time Plasma/Probe Behavior	53
5. SUMMARY OF RESULTS.....	55
APPENDIX A - TWO-FLUID PLASMA CODE.....	57
REFERENCES.....	70

LIST OF FIGURES

<u>Figure</u>		<u>Page</u>
1	Example of normal electron distributions at the extremes of the sunspot cycle at geomagnetic latitudes of 30 to 40°	9
2	Number densities of individual atmospheric constituents as a function of height for three representative exospheric temperatures	10
3	Experimental data of Cohen (Ref. 15) for ion beam emission from a rocket probe	12
4	Thermal electron current vs. electron density and temperature	19
5	Thermal ion current vs. ion density and temperature	20
6	Probe potential vs. electron beam current for different plasma environments	21
7	Probe potential vs. ion beam current for different plasma environments	22
8	Potential spatial variation away from probe.....	23
9	Sheath radius for electron beam emission and ionization mean free distance	24
10	Curves for estimating the onset of orbital limiting with no air ionization	24
11	Radial variation of potential for different ionization rates	32
12	Potential profiles for different emission currents	33
13	Probe potential versus beam current	34
14	Summary of treatment of ionization of neutral particles by electrons in the ABORC particle model for dynamic probe behavior.....	41
15	ABORC code model for a rocket-borne electron beam emission into a neutral plasma	43
16	ABORC particle calculations for probe potential time evolution for different electron densities.....	45
17	Effects of earth's magnetic field	47

List of Figures (Continued)

<u>Figure</u>		<u>Page</u>
18	Probe potential and plasma return currents calculated with and without the geomagnetic field	48
19	Maximum probe potential during the first 15 μ s calculated with and without the earth's magnetic field using the ABORC code particle model	49
20	Illustration of effects of beam pitch angle on system behavior	49
21	Probe potential calculated with and without ionization of a neutral background species	51
22	Early-time peak probe potential calculated with the ABORC particle model with and without secondary-electron production due to ionization of neutral species	53
23	Mesh geometry for code.....	59
24	Two-mesh zone problem.....	62
25	Average particle velocities as function of local potential, ϕ	65
26	Comparison of present code with analytical predictions from Reference 10 (no secondary emission from probe)	68

ABSTRACT

Analytical studies combining simple one-dimensional models with multidimensional computer codes have been performed to investigate charging characteristics of an emitting probe passing through a partially ionized neutral plasma. The effort is directed at predicting probe potentials as a function of emitted electron and ion currents for a variety of ambient plasma and neutral densities and temperatures corresponding to those found at altitudes between 80 and 400 km, where recent sounding rocket experiments have been performed. Calculations have been made for the early-time transient potentials and probe surface currents as well as for late-time or steady-state potential-current (I-V) probe characteristics. Efforts have been directed at explaining the apparently anomalously low probe potentials and local maxima in probe I-V characteristics which appear to occur only under conditions of electron emission.

Various possible effects previously identified were investigated, such as space-charge limiting of the emitted beam, enhanced local plasma produced by the emitting beams, rocket probe velocity, the earth's magnetic field, and sheath dynamics involving both space-charge limiting and orbit limiting of the return currents to the probe which act to neutralize the beam current. Most of these effects were investigated in the early-time regime ($t < 15 \mu s$) with the two-dimensional ABORC computer code, and virtually all of these effects except the enhanced local plasma tend to increase the probe potential for a given beam current. None appears to account for a local maxima in potential.

During the course of this effort, ionization of the neutral gas by the returning probe current (as opposed to the escaping beam current) was postulated as an important mechanism in the process. Analytical and numerical calculations indicate that this mechanism can be important in producing anomalously low potentials for electron current emission but not for ion current, apparently in agreement with rocket observations. It also can account for a local maximum in I-V characteristics. Calculations with the ABORC code in the early-time regime indicated only a small effect due to ionization, although potentials had reached a peak and were beginning to decline. Since late-time calculations could not be performed in a practical manner with the ABORC code, a one-dimensional analytical model was formulated to include effects of both space-charge limiting and ionization. The simplified steady-state model showed a considerable reduction in

predicted potentials for electron-beam emission with ionization, demonstrating that ionization of the background gas is a major factor in determining the probe potential in regimes where a significant gas density exists. For conditions that were investigated in some detail ($T_e \approx 1000^\circ\text{K}$, $N_{\text{plasma}} = 10^3/\text{cm}^2$, $N_{\text{neutral}} = 5 \times 10^{11}/\text{cm}^3$), the probe potential initially increased with increasing emission current. As the rate of ionization became significant with increasing emission current, the probe potential reached a maximum and then decreased at higher emission currents. For high neutral densities ($\sim 10^{12}/\text{cm}^3$) and relatively high emission currents ($\sim 0.1\text{ A}$), the probe potential appears to become pinned to the assumed ionization threshold (~ 40 to 50 eV). It should also be noted that the potential curve with respect to spatial position is very flat near the probe, so that the potential difference between the probe and a point located a few meters or less from the probe would be much less than the probe potential with respect to infinity.

1. INTRODUCTION

1.1 BACKGROUND

When an emitting probe is inserted into a partially ionized neutral plasma, it will attain a potential relative to the ambient plasma that is a function of several parameters, among which are the size and shape of the probe, probe velocity, plasma temperature and density, neutral gas density and species, magnetic field, beam current and voltage, and beam polarity. The relative importance of these parameters, the functional dependence of the probe current-voltage (I-V) characteristics on these parameters, and the way in which the beam couples to the ionosphere are not yet well understood.

To investigate these effects, a number of experiments involving sounding rockets in the upper ionosphere have been performed in which the rocket potentials have been measured for various ion and electron beam conditions. The literature describing these experiments is included in a companion literature summary report (Ref. 1). Results of these experiments indicate relatively high probe potentials (~ 850 V) for relatively low ion beam currents ($\sim 10^{-5}$ A), and relatively low probe potentials (~ 100 V) for relatively high electron currents (~ 0.1 A). In addition, there is some evidence that a local maximum in probe potential as a function of emitted electron current has been observed (Ref. 2).

Numerous analytical and computer calculations have been made in an attempt to explain the observed variation in probe potentials with altitude, emission current and species, and rocket orientation with respect to the geomagnetic field. Much of this literature is also described in Reference 1.

It appears that the probe potential for ion emission can be explained on the basis of Langmuir probe theory, including space-charge and/or orbit limiting, the theories of which are described in numerous references (see Refs. 3-5). These theories have to be somewhat modified to account for the geomagnetic field (Refs. 6-7).

The simple Langmuir probe theory does not account for the low observed potentials associated with electron emission, however. Most of the postulated effects which have not been treated in detail, such as the geomagnetic field, rocket velocity, and multidimensionality, would appear to result in higher probe potentials rather than in lower potentials. O'Neil *et al.* (Ref. 8), using Langmuir probe theory with an enhanced steady-

state electron concentration near the probe produced by ionization of the ambient background by the emitting beam, was able to arrive at relatively low potentials for electron beam emission.

This explanation is not entirely satisfying for several reasons, particularly for high-energy emitted beams. First, any ionization produced by the beam would be highly localized around the beam, and the one-dimensional Langmuir theory used in Reference 8 assumes a uniform enhanced distribution around the entire probe. Second, and just as important, the return current to the probe equals the emitted current in steady state and is of lower energy, often a few hundred electronvolts. The ionization rate produced by these low-energy returning electrons would be substantially higher than that occurring from the high-energy emitted electrons. Thus, ionization by the return current would dominate the ionization produced by the emitted current.

It is expected that the probe response would be considerably different, depending on which mechanism dominates. If ionization by the beam dominates, the return current to the probe would be largely confined to the region about the beam and the net beam current leaving the probe would be significantly smaller than the emitted beam current. Currents flowing on the rocket probe will be correspondingly small. If the return current is relatively uniform through the plasma, the net beam current will be approximately equal to the emitted beam current, and substantially higher replacement currents will flow on the rocket probe.

1.2 APPROACH

The main thrust of the present effort is to explore the mechanisms involved in beam coupling to the ionosphere, to quantify the probe I-V characteristics as a function of relevant physical parameters, and to identify a plausible mechanism which might explain a local maximum in the I-V characteristics for an electron-emitting probe.

During the course of these efforts, it became apparent that the ionization of the neutral background gas by electrons returning to the vehicle to balance the emitted current would play a dominant role in determining the probe potential. The main question is whether this process can produce the required magnitude of reduction in probe potentials at the densities of neutral plasmas corresponding to existing data, and whether the functional dependence of the potentials on the various physical parameters can be explained by this mechanism.

A two-fold approach was adopted with the aim of providing some quick order-of-magnitude estimates of the effects, along with a longer-term effort that would quantify the effects in more detail, perhaps in multidimensional geometries if necessary. These approaches included simple one-dimensional analytical steady-state models using Poisson equations with ionization of the neutral background by returning electrons, and a two-dimensional time-dependent computer code with space-charge limiting, ionization, and magnetic field effects. Near the end of this effort, a quasi-static two-fluid model of the electron and ion gas was employed in an attempt to overcome computational difficulties of the particle-pushing computer code and obtain two-dimensional time-dependent information.

The principal analytic treatment consisted of a steady-state solution of the Langmuir space-charge problem with ionization in spherical symmetry. Because of the spherical symmetry, these solutions cannot rigorously consider the effects of the geomagnetic field, the velocity of the probe, or the dynamics of the emission beam itself. In Reference 3, Lam presented a solution to the problem of an emitting spherically symmetric probe without ionization. This is one of the simplified models that predicted too large potentials for electron emission. To gain greater insight into the factors that influence the magnitude of the probe potential, this spherically symmetric model was reexamined under this program, with a slightly different outer boundary condition than the one used by Lam. A series solution was found for the potential in the sheath depletion region which agreed very well with Lam's numerical integration (Section 3). Unfortunately, it does not appear practical to include ionization effects and produce purely analytical solutions. Consequently, the equations were solved numerically for the sheath-region potential in a form that could later be extended to include ionization. As would be expected, the numerical results from the computer code without ionization are in reasonable agreement with the analytic results of Lam and, therefore, with the series solution. Consequently, these calculations also predict too large potentials for electron emission without ionization.

When ionization is added to the problem, the situation becomes much more complicated because the charge density at a particular radius from the probe is not just a function of the potential at that position, as it is in the simple models without ionization, but is a function of the ionization rate at all other points in space and of the potential difference from the point of interest to those positions. In other words, the charge carriers at a given location retain some memory of where and at what potential they were created.

To solve this problem, the previously developed numerical technique was extended to include ionization, as described in Section 3.4.2. The solution to the problem with ionization is computationally quite sensitive, especially for mean free ionization distances less than 10 to 100 m and large emission currents. The result is that the relatively simple iterative procedure used in the code would not always reach a fully converged solution. The difficulty undoubtedly could be improved with more refined iteration algorithms. However, at worst, the calculated results tend to oscillate about the apparently correct solution. The results clearly indicate that even a relatively low background gas density (relatively large ionization distance) can greatly reduce the probe potentials from the predicted values without ionization.

An alternate approach attempted late in this effort was a quasi-static time-dependent two-fluid computer model of the electron and ion gas, programmed in cylindrically symmetric coordinates using finite-difference techniques; this code was a relatively small modification to a previously existing code. It was to be utilized in an attempt to overcome the computational difficulties which arise in all particle-pushing codes, such as ABORC, when the particle densities become too large. One of its advantages over the steady-state models is that it could give the time evolution of the probe potential. In addition, it can treat more realistic cylindrical probes. Some early results gave promise that this code could be useful, especially in the high-density regimes. Unfortunately, no specific results were obtained at the time this report was prepared. Such an approach appears promising and will be pursued further. The physics and status of this technique are documented in Appendix A.

The computer code effort was initiated by a review of the known computer codes thought to be potentially useful for space plasma problems in general and the present problem in particular (Ref. 1). The "two-and-a-half"-dimension, cylindrically symmetric computer code ABORC (Ref. 9) contains many of the desirable features for the present problem and is reasonably economical to run. This code was modified to include the earth's magnetic field, an initial ionized background plasma, and ionization of the neutral gas by the emitted electron beam and the replacement plasma electrons. The advantage of this code is that its physics are quite rigorous, with a minimum of simplifying assumptions and approximations. Its main disadvantage is that, for computational reasons, it is practical to use this code only for early times ($t \lesssim 50 \mu s$) after the emission beam is turned on. In this time regime, it is adequate to simulate the positive ions as an immobile uniform background charge density, although that restriction is not inherently necessary in the ABORC code. The modifications that were made to the ABORC code specifically for this program are described in Section 4, along with the computations and results.

1.3 REPORT ORGANIZATION

The initial literature survey of analytic techniques, numerical computer codes, and rocket probe experiments is contained in a separate companion volume (Ref. 1). The ionospheric environments, including neutral and ion densities and temperatures as a function of altitude and time of day, are summarized in Section 2, along with a sample of the pertinent rocket probe data obtained for both ion and electron emission.

The steady-state analytic approach using Poisson's equation is described in Section 3. Comparisons to early work by Lam (Ref. 3) in the absence of ionization are also included. The principal results of this report, describing the effect of ionization of the neutral gas by returning electrons and the local maxima in the I-V characteristics, are also described.

The numerical results using the two-dimensional time-dependent ABORC code are described in Section 4. Comparisons are made with the one-dimensional numerical work of Rothwell (Ref. 10). The effects of ionization on the early-time response are reported, as well as the effects of the magnetic fields. One-dimensional and two-dimensional results are also compared.

The main results of the effort are summarized in Section 5. A short description of an alternate numerical approach thought to be capable of describing the time-dependent behavior of the rocket probe in two dimensions is summarized in Appendix A.

2. ENVIRONMENTS AND DATA FOR IONOSPHERIC PROBE EXPERIMENTS

This section briefly describes the ionospheric parameter ranges of interest to the present work, and surveys experimental data obtained from charged particle beam excitations by probes at various altitudes. Only the parameters relevant to the calculational modeling for probe potential are considered. Additional details of the environment are discussed in Reference 1.

At high altitudes, the sun's radiation causes appreciable photoionization of the atmosphere. At low gas pressures, recombination of the electrons and ions is slow enough that high electron concentrations can exist even through the night. Figure 1 shows typical day and night electron densities as a function of altitude for the extremes of the sunspot cycle. Above the F2 region, the electron density monotonically decreases out to several earth radii. Beyond several earth radii, at the outer edge of the protonosphere, the electron densities are determined by solar wind or interplanetary plasma. For 100- to 500-km ranges, the electron density varies from 10^3 to 10^6 e/cm³. The electron temperature can be as large as 1 eV, as discussed in Reference 1. Other less relevant plasma characteristics for the present purposes are also described there.

The density of neutral species is a strong function of height and exospheric temperature. Figure 2 shows different species concentrations as a function of altitude for three different temperatures. The "geometric height" corresponds to the local altitude of the distributions shown for a given latitude, and the "geopotential height" corresponds to the altitude at a given latitude of the same isopotential surface (Ref. 11). A reasonable maximum value is approximately 10^{13} neutrals/cm³ when all the species are added together at the 100-km height. It is reasonable to lump the species together in the present computer model because the cross sections for ionization by electrons are similar in magnitude and their dependence on electron energy. Notice also that a mean molecular mass of 30 for the neutrals gives the ions a mass of approximately 55,000 times the electron mass (corresponding to a velocity ~200 times slower for a given energy). Also, variations as a function of latitude or isopotential surfaces are not of prime concern here, but rather scoping the parameter range is important.

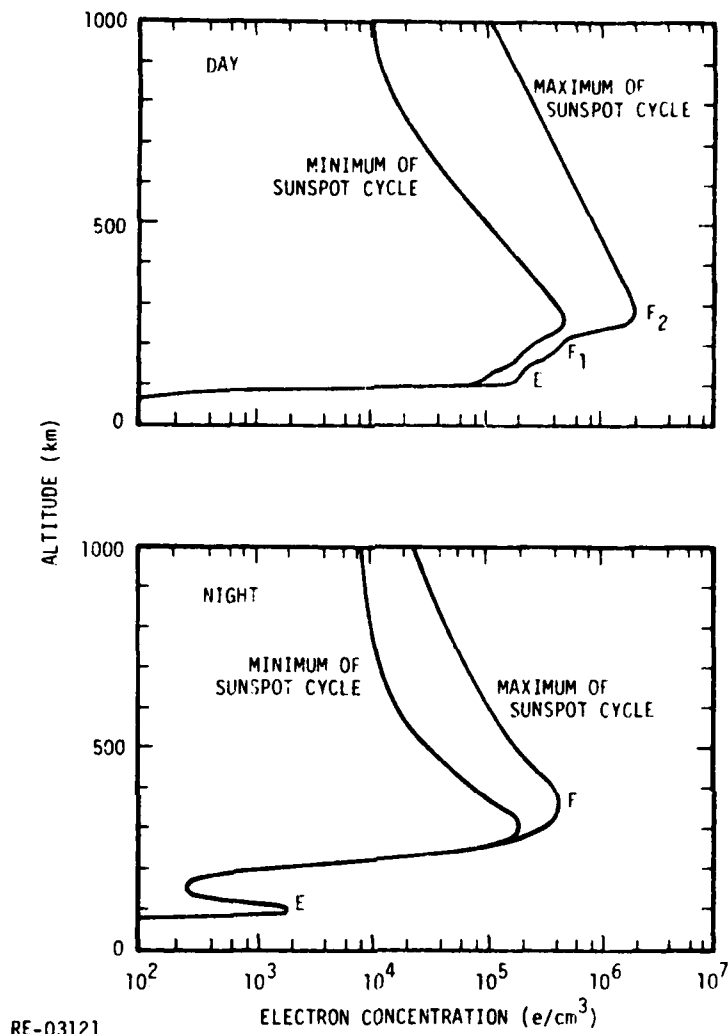


Figure 1. Example of normal electron distributions at the extremes of the sunspot cycle at geomagnetic latitudes of 30 to 40°. Curves are from Reference 12.

Ionospheric probe data from several experimenters is summarized in Table 1 and Figure 3. The table lists the experimental and environmental parameters. Both electron and positive ion beams of various currents (I) and energies (\mathcal{E}) were employed. A considerable altitude variation (h) resulted in a wide range of ambient electron densities (n). The temperatures and densities of the background environment are not provided in the references in several cases. Probable values from environmental graphs presented previously are indicated by a question mark in the table for those experiments. Perhaps

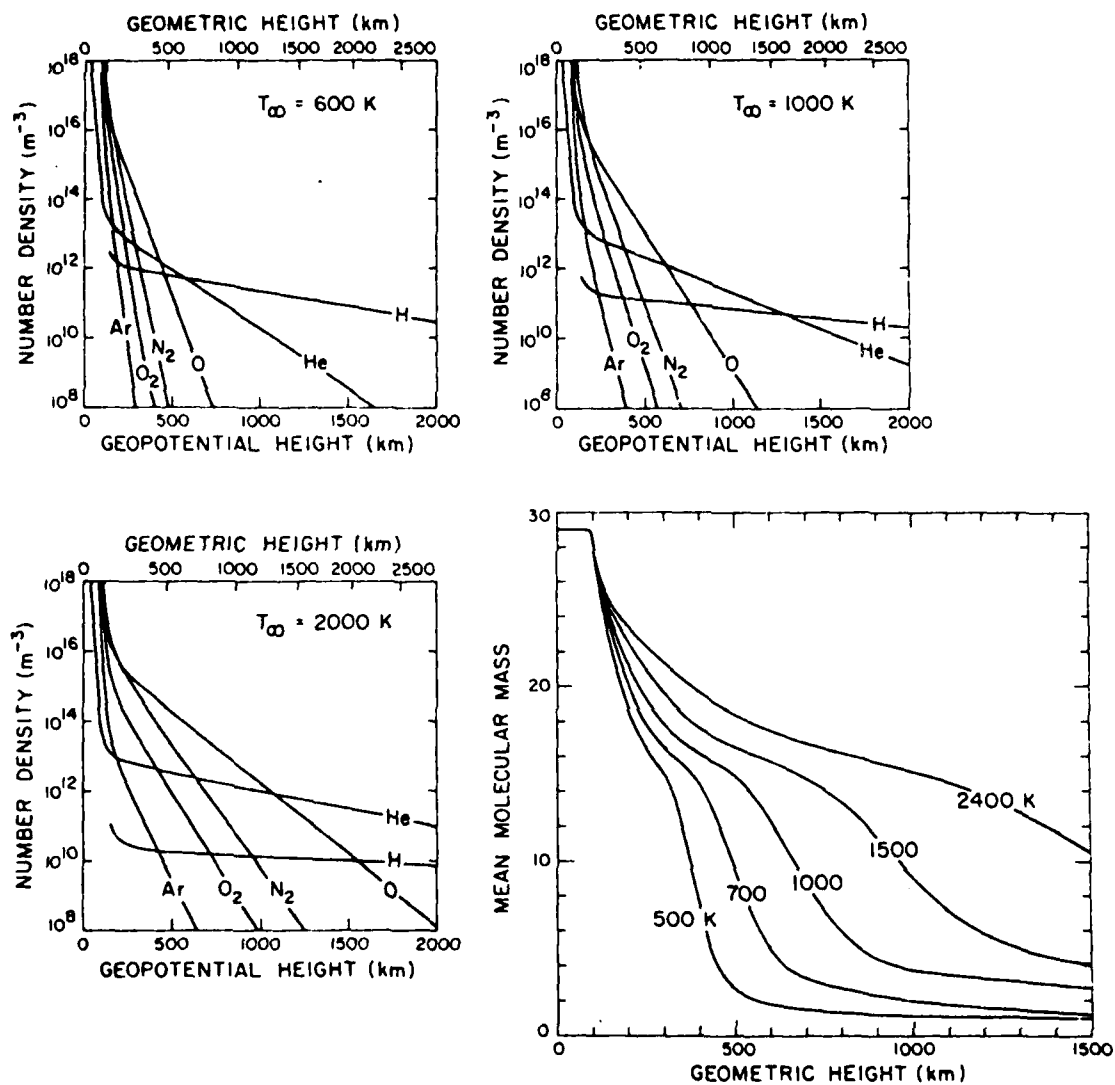


Figure 2. Number densities of individual atmospheric constituents as a function of height for three representative exospheric temperatures. The mean molecular mass as a function of height is shown for various exospheric temperatures in the lower right diagrams. Curves are from Reference 11.

the most striking result of the data is the tendency of the probe to linger at 100 V or less (as measured to ~3 m out from the probe in some cases) for electron beam emission. Ion emission at a much lower beam current than any of the electron-beam cases resulted in a potential at least 10 times higher for similar environmental parameters. Possible explanations for this behavior have included the background particle mass differences, the geomagnetic field, and the electron-neutral ionization cross section (which is maximum near 100 eV). The last item appears to be the major effect limiting the probe potential, as reported in Section 3. The ions have a much lower ionization cross section than the electrons, and allow the potential to increase further than an electron-beam case. The analytic theory of Lam (Ref. 3), which does not include ionization effects, was evaluated and found to be in reasonable agreement with the data for the ion case (see the data points in Figure 3). The analytical results are discussed further in Section 3.

Table 1. Ionospheric Probe Experimental Data Summary

Experimenter	Experimental Parameters				Environment Spec.			Rocket/Size	Date	Reference
	Beam Particles	I (A)	(eV)	ϕ_{probe} (V)	h (km)	n (#/cm ³)	T (eV)			
Cohen	e ⁻	several	3x10 ³	100	120	10 ³ ?	0.1?	?	1979?	Private comm. to H. Linnerud 3/80
Cohen	e ⁻	0.1	45x10 ³	100	350	2x10 ⁵ ?	0.1?	?	1979?	
R. O'Neil	e ⁻	0.8	2.5x10 ³	3-30	80-120	10 ³ ?	0.14	Precede 6 x 0.23 m	10/74	JGR 7/1/78 (Ref. 8)
Arnoldy/Winckler	e ⁻	0.07	4x10 ⁴	3-5	350?	2x10 ⁵	0.1?	Echo III	>1978	Arnoldy & Winckler, UNH rpt '78 (Ref. 13) Echo IV, Ref. 14
Cohen	e ⁻	0.01	90	90	150?		0.1?	White Sands 3 x 0.38 m	1/21/78	GRL 6/79, Cohen (Ref. 15)
Cohen	X _e ⁺ (Z=54)	1.2x10 ⁻⁵	2x10 ³	850	100-400	10 ³	0.1?	White Sands 3 x 0.38 m	1/21/78	GRL 6/79, Cohen (Ref. 15)
French-Russian	e ⁻ ?	0.5	1.5x10 ⁴	100	?	?	?	ARAKS	1974	Gendrin (Ref. 20)

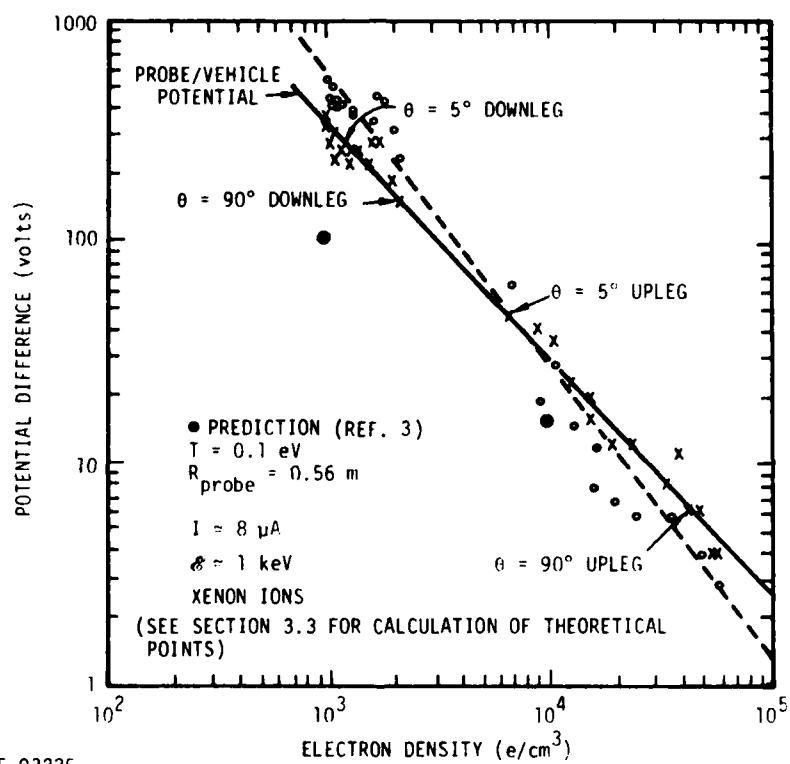


Figure 3. Experimental data of Cohen (Ref. 15) for ion beam emission from a rocket probe

3. SPHERICALLY SYMMETRIC STEADY-STATE MODEL

3.1 LAM'S MODEL

In Reference 3, Lam presented a steady-state analysis for a spherically symmetric emitting probe without ionization. His model is an extension of the Langmuir-Childs solution, using a different outer boundary condition. He divided the radial distance from the probe into three regions: (1) a quasi-charge-neutral outer region where the electron and ion densities are approximately equal, (2) an inner sheath region where the charge species that is repelled from the probe has essentially zero density, and (3) an intermediate transition region.

It is useful to repeat his mathematics for the sheath region since it is identical to the Langmuir-Childs model used for the series solution (Section 3.2) and nearly identical to what is used in the computer model without ionization in Section 3.4.1.

The potential ϕ at any point is governed by Poisson's equation:

$$\nabla^2 \phi = -\rho/\epsilon_0, \quad (3-1)$$

where ϵ_0 is the permittivity of free space and ρ is the charge density of the attached species, since the repelled species is assumed to be completely depleted from the sheath region. The density of the emitted particles is ignored here since their velocities are usually much greater than the returning particles and, hence, their densities are much less.

In steady state, the returning current must be continuous and equal to the emitted current:

$$I = -\rho v A = -4\pi \rho v r^2, \quad (3-2)$$

where positive I is an outward going current, v is the absolute velocity of the returning particles, and A is the area of an imaginary shell located at r .

Combining Eqs. 3-2 and 3-1,

$$\nabla^2 \phi = \frac{I}{4\pi\epsilon_0 r^2 v}. \quad (3-3)$$

In the sheath region, the potential will often be considerably greater than the initial thermal energy of the charged particles. In that case, the particle velocity v can be obtained by equating the kinetic energy of the particle to the electrostatic potential energy:

$$\frac{1}{2} m v^2 = e |\phi| \quad , \quad (3-4)$$

where m is the mass of the particle and e is the magnitude of the electronic charge. This assumption is sometimes called the "free-fall" approximation for the attracted species.

Combining Eqs. 3-4 and 3-3 gives

$$\nabla^2 \phi = \frac{1}{4 \pi \epsilon_0 \sqrt{\frac{2e}{m}} r^2 \sqrt{|\phi|}} \quad . \quad (3-5)$$

In the sheath region, Lam defines a dimensionless potential,

$$F = |\phi| \left(\frac{4 \pi \epsilon_0 \sqrt{2e}}{11 \sqrt{m}} \right)^{2/3} \quad , \quad (3-6)$$

and a dimensionless inverse distance,

$$\tau = r_0 / r \quad , \quad (3-7)$$

where r_0 is the outer radius of the sheath region. We have added the absolute value symbols in Eq. 3-6 to make the results apply to either electron or ion emission. In terms of these variables, Eq. 3-5 becomes

$$\tau^2 \frac{\partial^2 F}{\partial \tau^2} = \frac{1}{\sqrt{F}} \quad . \quad (3-8)$$

Lam integrates Eq. 3-8 numerically across the depletion region using a boundary condition at $r = r_0$ which he obtained by matching numerical solutions of his differential equations in the other two regions. His solution is reproduced here in Table 2.

Table 2. Tabulation of Function F(τ)

τ	F(τ) (from Lam)	F(τ) (from series solution)
1.0	0.0000	0.0000
1.01	0.00370	0.00369
1.02	0.00929	0.00927
1.03	0.01590	0.01591
1.04	0.02327	0.02322
1.05	0.03125	0.03123
1.10	0.07775	0.07767
1.15	0.13189	0.1319
1.20	0.19131	0.1912
1.25	0.25473	0.2545
1.295	0.31456	0.3144
1.30	0.32135	0.3212
1.50	0.610	0.6102
2.00	1.41	1.417
3.00	3.19	3.173
10.00	16.4	16.28
100.0	188.0	188.17

3.2 SERIES SOLUTION IN SHEATH REGION

If the outer two regions in Lam's analysis are ignored and ϕ is taken to be zero at $r = r_0$ (as is done in the computer model in Section 3.4), a solution to Eq. 3-8 can be obtained exactly in terms of a series solution:

$$F = A_1 \ln^{4/3} \tau + A_2 \ln^{7/3} \tau + A_3 \ln^{10/3} \tau + \dots \quad (3-9)$$

This series automatically satisfies the two boundary conditions that the potential (F) and the electric field ($\partial F / \partial r$) are zero at the outer boundary of the sheath ($\tau = 1.0$). The constants A_i can be evaluated by substituting Eq. 3-9 into Eq. 3-8 and equating equal powers of $\ln \tau$ on both sides of the equation. The result is

$$F = 1.7171 \ln^{4/3} \tau + 0.68684 \ln^{7/3} \tau + 0.20605 \ln^{10/3} \tau + 0.04766 \ln^{13/3} \tau \\ + 0.00894 \ln^{16/3} \tau + 0.00141 \ln^{19/3} \tau + \dots \quad (3-10)$$

The series in Eq. 3-10 may be convergent for all values of $\ln \tau$ since the coefficients of $F/1.7171 \ln^{4/3} \tau$ shown in Eq. 3-10 are smaller than those in the expansion of $(e^v - 1)/v$, $v = \ln \tau$.

However, we have not rigorously proven that the higher order terms are convergent. Consequently, this series will only be used for $0 < \ln \tau < 1$, where it is clearly convergent.

If the ratio of the sheath radius to the probe radius is not too large (that is, $r_0/R \lesssim 2.718$), Eq. 3-10 can be used for the potential profile throughout the sheath region. For values of $r_0/R > 2.718$, another series solution, which also satisfies Eq. 3-8, can be used:

$$F = B_1 \tau + B_2 + B_3 \tau^{-1/2} + B_4 \tau^{-3/2} + B_5 \tau^{-2} + B_6 \tau^{-5/2} + B_7 \tau^{-3} + B_8 \tau^{-7/2} + B_9 \tau^{-4} + \dots \quad (3-11)$$

Note that the terms $\tau^{+1/2}$ and τ^{-1} do not appear in this series. If this series and the first derivative of F with respect to r are convergent for $\tau = 1.0$, Eq. 3-11 can be used throughout the sheath region from $r = r_0$ to $r = R$. The coefficients B_i ($i \geq 3$) can be obtained in terms of B_1 and B_2 by inserting Eq. 3-11 into Eq. 3-8 and equating coefficients of equal powers of τ on the two sides of the equation. B_1 and B_2 can then be obtained using the boundary conditions for the potential and the electric field at the outer edge of the sheath region (both = 0). However, if these series are not sufficiently convergent at $\tau = 1.0$, Eq. 3-10 can be used for the potential profile for $1 < \tau < 2.718$, and Eq. 3-11 can be used for $\tau > 2.718$. The coefficients B_1 and B_2 can then be obtained by matching the magnitude and first derivative of Eq. 3-11 to the magnitude and first derivative of Eq. 3-10 at some arbitrary value of τ such as $\tau = 2.718$, where Eq. 3-10 is still valid and Eq. 3-11 is more convergent than at $\tau = 1.0$. This is the procedure that has been used here. The resulting values for the first few B coefficients and the analytic relations of B_i ($i \geq 3$) to B_1 and B_2 are given below.

$$B_1 = 1.9123$$

$$B_2 = -3.1532$$

$$B_3 = \frac{4}{3} B_1^{-1/2} = 0.9642$$

$$B_4 = -\frac{2}{15} B_2 B_1^{-3/2} = 0.159$$

$$B_5 = -\frac{1}{12} B_3 B_1^{-3/2} = -0.0304$$

$$B_6 = \frac{3}{70} B_2^2 B_1^{-5/2} = 0.0843$$

$$B_7 = -\frac{1}{24} B_4 B_1^{-3/2} + \frac{1}{16} B_2 B_3 B_1^{-5/2} = -0.0424$$

$$B_8 = -\frac{2}{63} B_5 B_1^{-3/2} + \frac{1}{42} B_3^2 B_1^{-5/2} - \frac{5}{252} B_2^3 B_1^{-7/2} = 0.0727$$

The value of F vs. τ from these two series solutions (Eq. 3-10 for $\tau < 2.718$ and Eq. 3-11 for $\tau > 2.718$) are compared to Lam's results in Table 2. The agreement is very good over the whole range of τ in the table.

3.3 ANALYTICAL RESULTS

The above results have been used to generate some useful parametric curves. From Eq. 3-6, the probe potential (at $r = R$), relative to infinity, is given by

$$\phi_\infty \equiv |\phi(R)| = \left[\frac{\sqrt{m}}{4\pi\epsilon_0 \sqrt{2e}} \right]^{2/3} |I|^{2/3} F(r_0/R) . \quad (3-12)$$

For relatively large emission currents I (and therefore large probe potentials ϕ), the outer boundary of the sheath region r_0 can be assumed, with acceptable accuracy, to be the radial position where the inward thermal current of the attracted carriers just equals the emission current:

$$I = JA = -n_0 q v_{th} 4\pi r_0^2 , \quad (3-13)$$

where $v_{th} = (kT/2\pi m)^{1/2}$, n_0 is the density of the attracted species in the bulk, q is its charge (+ for ions, - for electrons), kT is its thermal energy, and v_{th} is the average velocity of the total density n_0 crossing a plane in one direction. If one considers only the half of n_0 whose velocities are directed toward a given plane, their average velocity toward the plane is

$$\sqrt{\frac{2kT}{\pi m}} .$$

Solving Eq. 3-13 for r_0 , the value of τ corresponding to the probe radius R is

$$\tau_p = r_0/R = \sqrt{\frac{-I}{4\pi R^2 q v_{th} n_0}} . \quad (3-14)$$

Note that $-I/q$ is always a positive quantity.

For purposes of numerical evaluation, we take the typical ion mass here to be 46,000 times the electron mass, which corresponds to a mean molecular mass of about 25, based on Figure 2 for an altitude of about 150 km. With this mass, the potentials become

$$\psi = 6.1 \times 10^2 I^{2/3} F(r_0/R) \quad (3-15)$$

and

$$\psi = -2.2 \times 10^4 |I|^{2/3} F(r_0/R) \quad (3-16)$$

for electron and ion emission, respectively.

It is convenient to specify explicitly the function $F(r_0/R)$ in terms of the current I . To do this, we introduce a current I_0 , defined as the current due to the thermal electrons which would strike the probe if the probe potential were zero, and thus the bulk plasma densities and velocities extended all the way into the probe and radius R :

$$I_0 = -4\pi R^2 q n_0 \left(\frac{kT}{2\pi m} \right)^{1/2}. \quad (3-17)$$

Taking the square root of the ratio of Eqs. 3-13 and 3-17,

$$\frac{r_0}{R} = \sqrt{\frac{I}{I_0}}.$$

The quantity I_0/R^2 is shown in Figures 4 and 5 for electrons and for ions with a mass $m_i = 46,000$ times the electron mass m_e , respectively, as a function of n for various temperatures. The I-V characteristics for the probe are shown in Figures 6 and 7 for various values of I_0 which in turn depends on R , T , and n .

It is interesting to use these curves to predict the potentials for typical experimental conditions listed in Table 1 and Figure 3. For electron emission, use an emission current $I = 0.1$ A with a plasma density $n = 2 \times 10^5/\text{cm}^3$ and a temperature $T = 0.1$ eV, and assume an effective probe radius of 0.5 m. From Figure 4, $I_0/R^2 = 0.022$ A/m², so $I_0 = 5.5 \times 10^{-3}$ A. From Figure 6, $\phi_\infty \approx 900$ V, which is considerably larger than the potentials measured by Cohen and by Arnoldy/Winckler for comparable conditions (Table 1). For ion emission, use $I = 1.2 \times 10^{-5}$ A, $n = 10^3/\text{cm}^3$, $T = 0.1$ eV, and $R = 0.5$ m. From Figure 5, $I_0/R^2 = 5 \times 10^{-7}$ A/m², so $I_0 = 1.25 \times 10^{-7}$ A. From Figure 7, $\phi_\infty \approx 300$ V, which is in fair agreement with Cohen's data in Table 1 for ion emission (850 V), considering the uncertainties in the environment conditions and the average value for R .

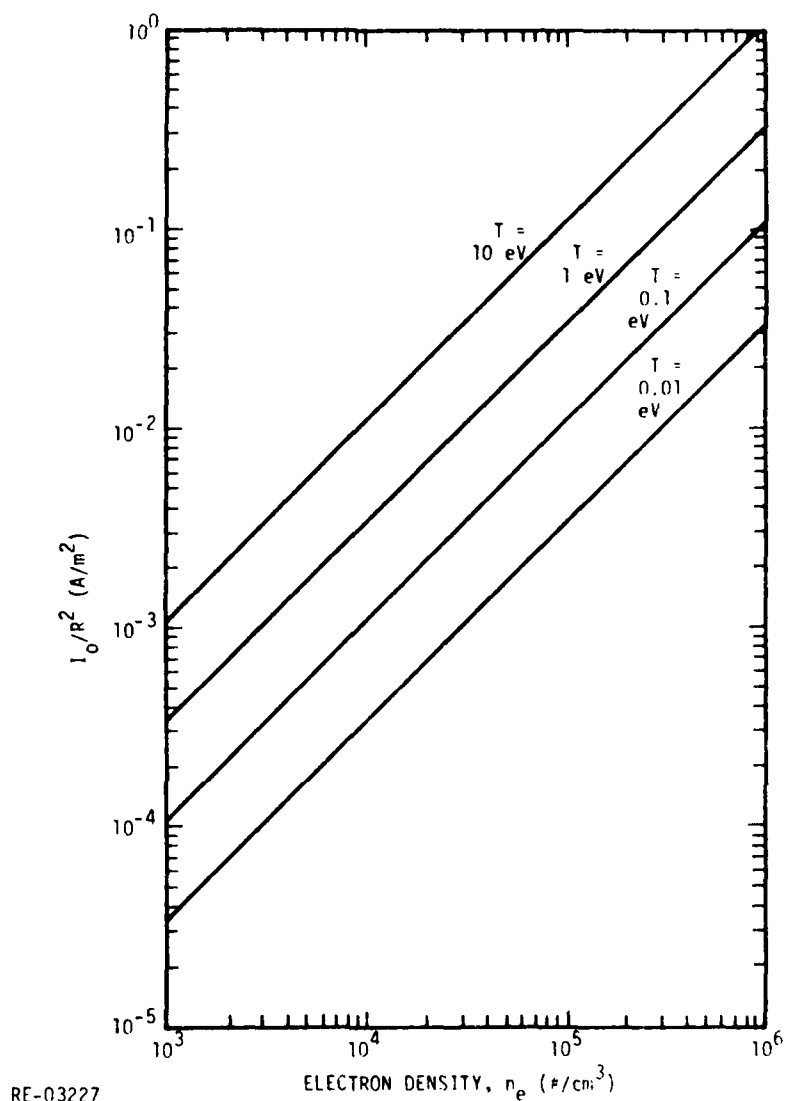


Figure 4. Thermal electron current vs. electron density and temperature

For the theoretical data points in Figure 3, an effective spherical probe radius of 0.56 m was used to give the same total probe area as on the cylindrical probe used in the Cohen experiments (Ref. 15). As noted later, this assumption could help to explain why the theoretical values are somewhat less than the measured values. The mass of the returning ions was assumed to be 46,000 times the electron mass, consistent with Eq. 3-16.

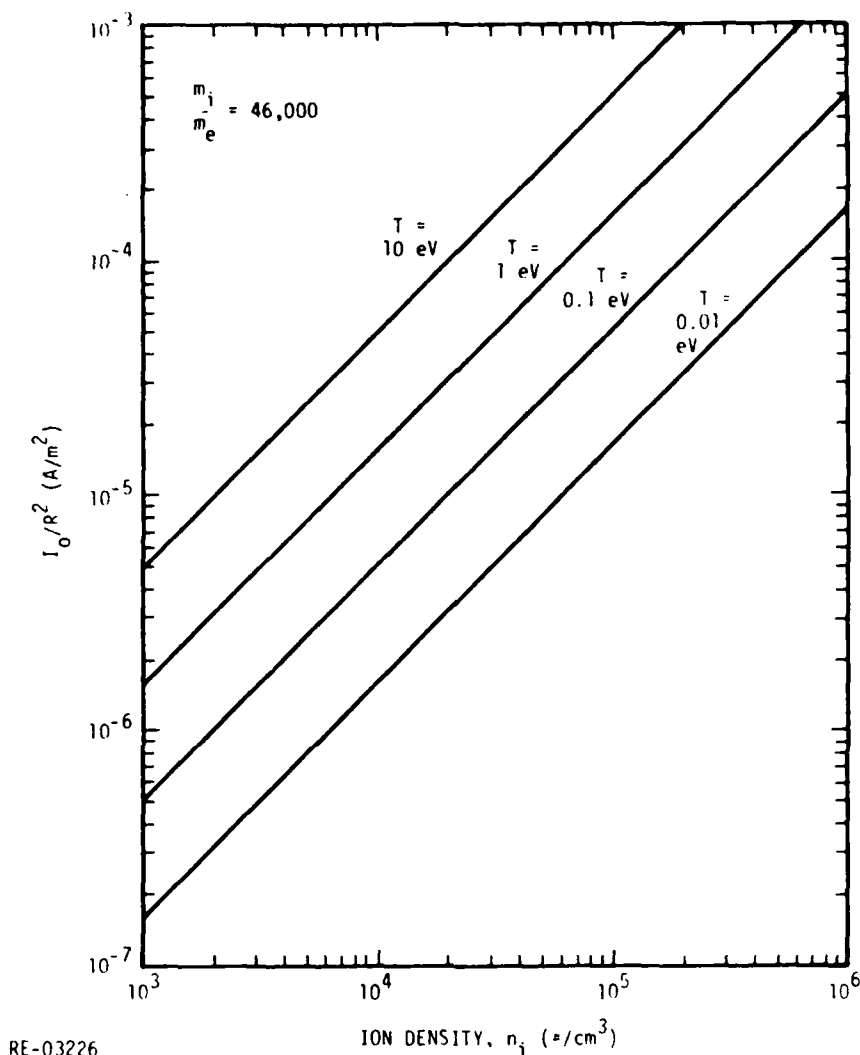


Figure 5. Thermal ion current vs. ion density and temperature

For the emission current of $8 \mu\text{A}$ in Figure 3, the outer radius of the sheath region (r_0) is 4 m, 1.26 m, and 0.4 m for bulk ion densities of 10^3 , 10^4 , and $10^5/\text{cm}^3$, respectively. Equation 3-16 and Table 2 (or Figures 5 and 7) then yield the theoretical potentials from the probe to infinity shown in Figure 3 for $n_0 = 10^3$ and $10^4/\text{cm}^3$. It should be noted that the 4 m sheath radius for $10^3/\text{cm}^3$ is outside the range of the potential-measuring device used in Reference 15. Hence, for a direct comparison to the experimental data in Figure 3 at $10^3/\text{cm}^3$, the calculated potential should be reduced somewhat. Since the value of $r_0 =$

0.4 m for $10^5/\text{cm}^3$ is less than the assumed probe radius of 0.56 m, the simple Lam theory obviously cannot be applied at this higher density. The difficulty is in the assumed radius of the spherical probe corresponding to the same area as the actual cylindrical probe. At the high densities where r_0 is quite small, it would be more logical to use an effective spherical probe with a radius closer to the radius of the cylindrical probe (0.19 m). Using a radius of 0.19 m for the spherical probe at a density of $10^5/\text{cm}^3$, Lam's theory yields a potential of about 12 V, which is considerably larger than the experimental values. This calculation just illustrates the rather obvious conclusion that, when the sheath radius is not too much larger than the probe dimensions, the detailed shape of the probe becomes more important and one should use a more correct geometrical model of the probe, if possible. Even at the lower densities, a smaller effective radius for the probe would increase the calculated potentials, bringing them into closer agreement with the measured values.

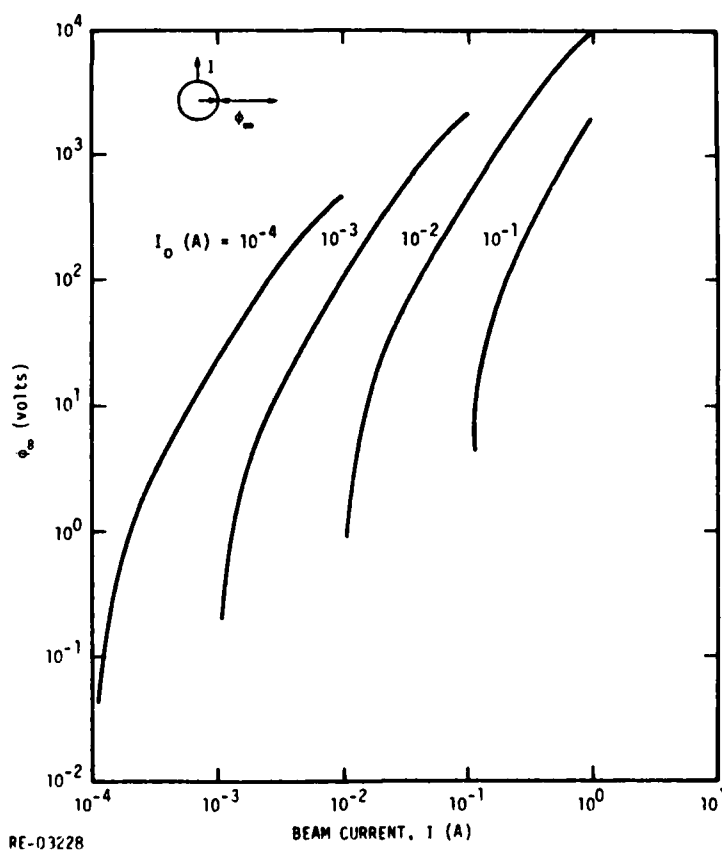


Figure 6. Probe potential vs. electron beam current for different plasma environments

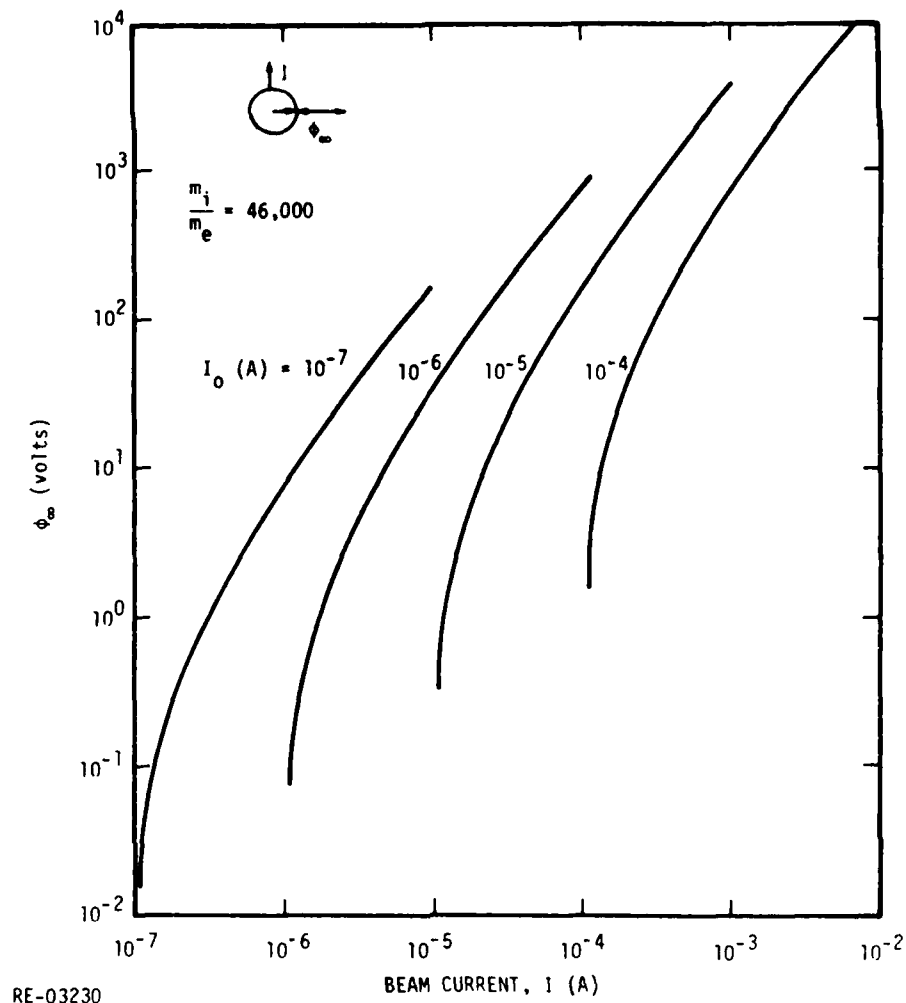


Figure 7. Probe potential vs. ion beam current for different plasma environments

The relative potential as a function of radial distance is shown in Figure 8. The potential is set equal to zero at $r/r_0 = 1$, that is, when r is at the virtual cathode located at $r = r_0$. The potential rises until the probe is reached at $r = R$.

Some additional curves that can be useful for planning probe experiments are given in Figure 9. One curve shows the mean ionization path length (λ) versus the density (N) of the neutral background air molecules for the peak ionization cross section (assumed to be $2 \times 10^{-16} \text{ cm}^2$). The significance of this parameter is discussed in Section 3.4.2. The other set of curves shows the radius (r_0) of the sheath region as a function of the bulk plasma density (n) and the emission current of electrons (I) for a plasma electron

temperature of 1000°K . For ion emission, the r_0 values in Figure 9 should be multiplied by $\sqrt{m_i/m_e}$. The equation shown on the figure for $\phi_{O.L.}$ is the probe potential at which orbital limiting starts to occur. It is obtained from Eq. 3-21 in Section 3.5 by solving for ϕ , letting $p = r_0$, and identifying $1/2 m v_0^2$ with kT . For values of probe potential $\phi_\infty > \phi_{O.L.}$, all electrons that start at r_0 with a component of velocity pointing toward the probe will be captured by the probe and thus there is no orbital limiting. However, for $\phi_\infty < \phi_{O.L.}$, some of the electrons that start at r_0 will circle about the probe without striking it, which means orbital limiting does occur. This figure and equation are applicable even if ionization of the neutral atoms occurs and reduces the probe potential below the Lam value for no ionization, as discussed in Section 3.4. A similar set of curves that is only applicable without ionization is shown in Figure 10. In this figure, at the probe potential corresponding to a given current and r_0/R , if r_0/R is less than the impact parameter p/R , orbital limiting will not occur. For example, for $I = 0.01\text{ A}$ and $\phi_\infty = 1000\text{ V}$, $r_0/R \approx 20$. If $kT = 1\text{ eV}$, $p/R \approx 30$, so orbital limiting does not occur. On the other hand, for $kT = 10\text{ eV}$, $p/R \approx 10$, so orbital limiting would occur.

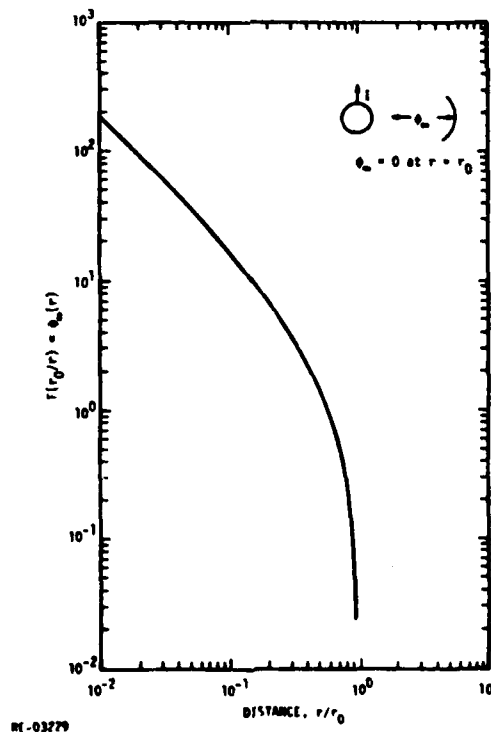


Figure 8. Potential spatial variation away from probe

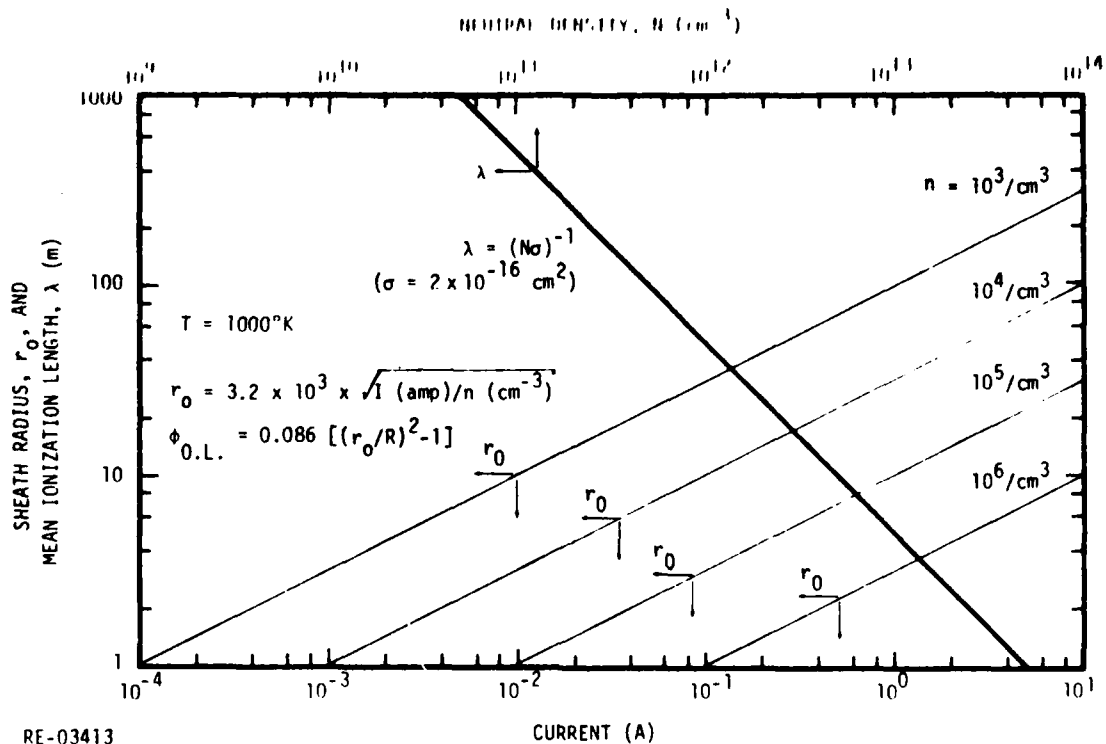


Figure 9. Sheath radius for electron beam emission and ionization mean free distance

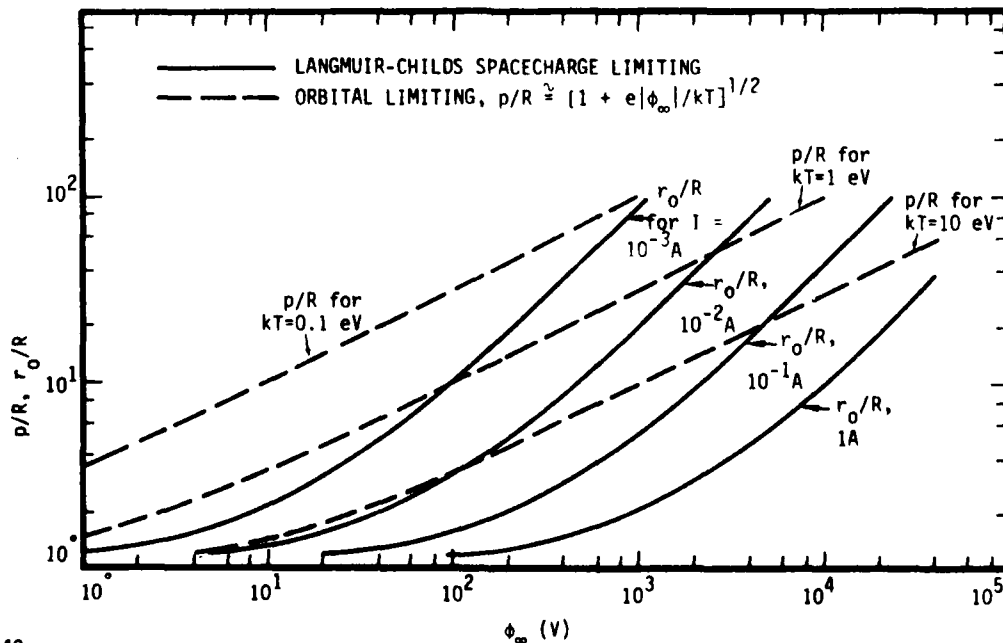


Figure 10. Curves for estimating the onset of orbital limiting with no air ionization

3.4 COMPUTER MODEL AND RESULTS

In the following discussion, the emitted, and therefore the attracted particles are taken to be electrons because ionization effects will normally be important only for electron emission and the main purpose of this code is to study ionization effects.

3.4.1 Model Without Ionization

The computer model without ionization is very similar to Lam's model in the depletion region. The only differences are in the outer boundary condition and a slight difference in the equation for the electron velocity.

In this model, the outer boundary of the problem is taken to be the edge of the depletion region. Instead of having a smooth transition from the depletion region to the bulk, as in Lam's model, the present model assumes a sharp transition from the depletion region, where the ions are completely swept out, to the bulk region where the ion density is equal to the bulk density. This approximation, which is the same one used for the series solutions in Section 3.2, is justified for relatively high electron emission currents, where the potentials are relatively large compared to the ion thermal energy and the sheath region is large compared to the transition region. Since the net charge outside the depletion region boundary is assumed to be identically zero, the electric field at the boundary is zero, and the potential ϕ is defined to be zero at that point. A central element of this model is that the outer edge of the sheath is given by the condition that the inward electron thermal current just equals the electron emission current (Eq. 3-13).

The second difference between the computer model and Lam's model and the series solutions is that the radial electron velocity at a position where the potential is ϕ is given in the code by

$$v_e = \sqrt{v_{th}^2 + 2e\phi/m} . \quad (3-18)$$

where e is the absolute value of the electronic charge. This difference from the electron velocity in Eq. 3-4 is significant only close to r_0 where ϕ is very small. If Eq. 3-4 were used instead of Eq. 3-18, the carrier densities ($\sim 1/4\pi r^2 v_e$, Eq. 3-2) close to r_0 would be considerably greater than the bulk density n_0 , and the average radial velocity v_e would be correspondingly less than v_{th} . The use of Eq. 3-18 ensures a smooth variation of n_e across the boundary region. No analysis has been performed to determine how much this change affects the overall probe potential. However, since it was convenient and easy to incorporate into the code, this change has been utilized.

With no ionization, it is a straightforward matter in the code to integrate Poisson's equation inward, starting from the sheath boundary $r = r_0$, where ϕ and the electric field

both equal zero in this model. Using a finite-difference mesh grid where the potentials, and consequently the velocities and carrier densities, are defined on the mesh points and the electric fields are defined at the half-mesh points, the integration can proceed from mesh to adjacent mesh, from $r = r_0$ to the probe radius, $r = R$.

Table 3 shows a comparison of calculated probe potentials obtained with this code (with no ionization and with fully depleted ions in the sheath region) with results from Lam. The agreement is quite satisfactory considering the differences in the two models.

Table 3. Comparison of Results from Computer Model with Lam

Plasma Density = $10^3/\text{cm}^3$			
Electron Thermal Energy (eV)	Emission Current (A)	Potential (V) for 1-m-radius probe	
		Lam	Computer Model (No ions or ionization)
10.0	6×10^{-3}	28	28.5
10.0	6×10^{-2}	852	960
0.1	6×10^{-3}	184	230

With the computer model, it is also possible to simulate the condition of electron emission and an electron return current with a fixed background of positive charge equal to the bulk ion density. This calculation would correspond to the early-time ABORC calculations before the ions have had time to be swept out of the sheath region. Table 4 shows a comparison of the probe potentials from this code for fixed and swept-out ions and with the corresponding ABORC calculations with fixed ions. The comparison of the fixed-ion results with ABORC is quite good for large emission currents, especially considering the differences in the geometry and calculational techniques. The reason for the differences at low beam currents is not known for sure, but one possibility is orbital limiting, which is present in ABORC but not in the steady-state code. From Figure 10, for $I = 6 \times 10^{-3}$ A and ϕ between 7 and 30 V, the curve for r_0/R is above the curve of p/R for $kT = 10$ eV. Hence orbital limiting is occurring for this case and the potentials should be larger than predicted by the steady state theory. Therefore, it is reasonable that the ABORC code should give a larger potential for this case. As discussed in Section 3.5, the orbital-limiting effect is largest when the electron thermal energy is relatively large compared to the probe potential, as is the case for the lower emission currents in

Table 4. For more realistic thermal energies (~ 0.1 eV), this effect should be less important even for probe potentials as low as 10 eV.

Table 4. Effect of Stationary Ions

(Plasma Density = $10^3/\text{cm}^3$)				
Electron Thermal Energy (eV)	Emission Current (A)	Probe Potential (V)		
		Steady-State Code, 1-m-radius Sphere		ABORC, 1-m-radius cylinder Fixed Ions
		Ions Swept Out	Fixed Ions	
10	6×10^{-3}	28.5	7.6	30
10	6×10^{-2}	960	165	280
10	0.6	15 kV	2.2 kV	2.7 kV
0.1	6×10^{-3}	230	8.6	--

It is interesting that the predicted potentials with the fixed ions are considerably smaller than the predicted potentials when the ions are assumed to be completely swept out of the sheath region. The physical reason for these lower potentials is fairly clear from the code calculations. When the ions are not present, the electron density tends to be less than in the bulk, in spite of the $1/r^2$ geometry effect, as the probe potential accelerates the electrons toward the probe. On the other hand, with the ions present, the electron density tends to stay roughly equal to the ion density. Therefore, to supply the same return current, the high-density electrons in the fixed-ion case do not have to move as rapidly as the low-density electrons in the fully depleted case, and thus, the probe potential can be smaller. This difference in potential should be observable in a time-dependent calculation, and perhaps in an experiment with a low emission current and small probe potential such that ionization is not a major effect. When the electron beam is first turned on, the probe potential should quickly rise to a plateau corresponding to the fixed-ion case. Then, on a time scale corresponding to the ion sweepout time, the probe potential should gradually rise toward the value in the fully depleted case. However, this time-dependent effect might be obscured when ionization effects are large and have a major influence on the probe potential, as discussed in the next section.

The important result from this analysis is that the predicted potentials in Table 3 with movable ions are considerably larger than the measured probe potentials with electron emission (Table 1). Therefore, some important physics is apparently missing from the non-ionization model used thus far.

3.4.2 Model with ionization

When an electron in air achieves a kinetic energy greater than the ionization energy of the air molecules, there is a finite probability that it will produce additional electron-ion pairs. If this ionization occurs in a region where an electric field exists, the newly created electrons and positive ions will be accelerated in opposite directions, and thus, both species will contribute to the electric current. If the electric fields are large enough over a sufficient distance, the new electrons will reach a kinetic energy greater than the ionization energy and, thus, can produce additional ionization. This multiplying effect is known as avalanching.

To simulate ionization effects in the steady-state computer code, the ionization probability curve versus electron energy was approximated as a linearly increasing curve starting at 50 eV and going to 200 eV. Above 200 eV, the probability curve was assumed to be flat for all higher energies. To smooth the calculations near the discontinuities at 50 and 200 eV, a smooth parabolic transition was used, extending 10 eV on either side of each discontinuity. This assumed ionization curve has a somewhat higher threshold energy than the experimental curve for oxygen in Figure 14 (see Section 4). It is believed that the detailed shape of this ionization curve will not have a major effect on the computed results. However, this shape could be easily modified for other calculations if desired. The peak magnitude of the probability curve is an input parameter in the code corresponding to different densities of the neutral background gas. This parameter is given in terms of the mean distance for ionization (λ) by an electron with energy greater than 200 eV -- that is, with the maximum ionization probability.

Ionization can come from three different sources of electrons: (1) emitted electrons, (2) return electrons which originate at the outer boundary of the sheath region, and (3) electrons created by the ionization which are then accelerated to energies above the ionization threshold. In the present code, ionization by the emitted electrons is ignored because their density, when averaged over a spherical shell around the probe, is considerably less than the density of the returning electrons. Also, the energy of the emitted electrons is often quite high, and the ionization probability actually decreases at high energies, contrary to what was assumed above for the code.

When the code was first being written, it was intended to include ionization by the newly created electrons which are then accelerated to the ionization threshold. However, some calculations with an earlier, simpler version of the code indicated that, whenever ionization is significant, the potential curve becomes relatively flat and the ionization electrons seldom reach the energy for the ionization threshold. Therefore, ionization by these electrons, that is, avalanching, has been omitted from the code for simplicity, although it could be added with not too much complexity if it were thought to be important. Thus, only ionization by the electrons which return from the outer boundary of the sheath are included in the code.

Ionization is incorporated into the code as a carrier generation rate, dn/dt , in each mesh region proportional to the density of electrons passing through that zone and as a function of their local energy. Both the electrons and the ions are assumed to be created with zero initial velocities. In steady state, dn/dt at a specific mesh station j will contribute to the electron current and density at all mesh stations i closer to the probe than j , and to the ion current and density at all mesh stations k further from the probe than j .

The velocity of the electrons from region j when they reach region i is taken to be

$$v_e(i) = \sqrt{\frac{2e}{m_e} [\phi(i) - \phi(j)]} , \quad (3-19)$$

where $\phi(i)$ and $\phi(j)$ are the potentials at regions i and j . (In the sign convention used in the code, the potentials are positive for electron emission.) Since physical reasoning indicates that the potential curve must increase monotonically from the outer edge of the sheath to the probe, the argument of the square root in Eq. 3-19 is always positive.

If there were no sweepout velocity due to the motion of the probe relative to the ambient plasma, the velocity of the ions from region j when they reach region k would be given by an equation similar to Eq. 3-19 but with $\phi(i)$ replaced by $\phi(j)$, $\phi(j)$ replaced by $\phi(k)$, and m_e replaced by the ion mass m_i . It is not possible to simulate rigorously a linear sweepout velocity in a spherically symmetric geometry. However, in an admittedly rather crude attempt to include some effect of sweepout, the ions were given an additional radial outward velocity v_s . Thus, the ion velocity at position k was calculated from the formula

$$v_i(k) = \sqrt{v_s^2 + \frac{2e}{m_i} [\phi(j) - \phi(k)]} . \quad (3-20)$$

For all of the results presented later, the magnitude of m_i was taken to be $2 \times 10^4 m_e$ and v_s was taken to be 5000 m/s, which is probably somewhat high for typical probe velocities. However, again it is felt that this value would not have a major effect on the conclusions from this study. If desired, the magnitude of v_s could be changed for future calculations.

The charge density ρ in Poisson's equation (Eq. 3-1) is the algebraic sum at each mesh position of the densities from the inward-bound electrons that originally crossed the outer boundary of the sheath region (as in the zero-ionization case) and the electrons and ions created by the ionization process.

The steady-state solution to this problem with ionization is mathematically very sensitive at high emission currents and relatively small mean ionization distances ($\lambda \lesssim 100$ m). The reason is that the potential curve with heavy ionization becomes very flat after the potential reaches the ionization threshold around 50 eV. Therefore, the velocities of the electrons and ions that were created by the ionization due to the returning electrons (Eqs. 3-19 and 3-20) become quite small and the corresponding densities become very large. To solve this problem even for values of λ as large as 1000 m, it was necessary to use a calculational approach which inverts a linearized $2N \times 2N$ matrix, where N is the number of mesh regions used in the calculations, typically about 100. The factor of 2 occurs because both ϕ and its derivative (E) are used as variables. Since the equations are very nonlinear, the procedure used is to estimate initial potential and electric field curves over all of the meshes. The equations are then linearized for perturbations in ϕ and E from these initial curves. This linearized matrix is then inverted to obtain the changes in E and ϕ .

In principle, one would like to use these new curves for ϕ and E around which to again expand the equations and, thus, repeat the process until the calculated changes in E and ϕ are less than some selected limit. Unfortunately, the new calculated ϕ curve is often not monotonically increasing across the sheath region. Consequently, this curve cannot be used since Eq. 3-19, and perhaps Eq. 3-20, would give imaginary velocities. Thus, after the linearized changes to E and ϕ have been calculated, some other algorithm is needed to choose a new estimated ϕ curve that is monotonically increasing. There is an infinite number of ways this could be done, since any procedure that is convergent should theoretically arrive at essentially the same converged result. The procedure that has been used is to adjust the old values of E by some fraction $F1$ of the calculated perturbations in E at every mesh station, provided that the new adjusted E is not negative. If any new E were negative, the old (positive) E at that mesh is reduced by some fraction $F2$ of its

value. These estimated E's are then integrated from r_0 inward to obtain the corresponding potential curve about which the equations are again expanded. There is no guarantee that this procedure will always be stable, especially if F1 and/or F2 are made too large in an attempt to speed up the convergence. In fact, at large currents and small λ 's, it was often difficult to obtain satisfactorily converged solutions. If this code were to be used in the future for those more difficult situations, this adjustment algorithm should be reviewed and perhaps modified.

All the calculations with this code thus far have been for an ambient ionized plasma density of $10^3/\text{cm}^3$ and an electron temperature of 1000°K ($kT = 0.086 \text{ eV}$). Figure 11 shows curves of the calculated potential versus distance from the probe for an emission current of 0.1 A, with no ionization ($\lambda = \infty$) and $\lambda = 1000$ and 100 m. Note in particular the flatness of the potential curve for $\lambda = 100 \text{ m}$ and how far the plateau extends from the probe. Assuming a peak value for the ionization cross section of $2 \times 10^{-16} \text{ cm}^2$, a value of $\lambda = 100 \text{ m}$ corresponds to a density of neutral background atoms of $5 \times 10^{+11}/\text{cm}^3$. A similar calculation for $\lambda = 10 \text{ m}$ did not completely converge, but the plateau potential was approximately 50 eV. Based on experience with the other λ 's, it is expected that essentially this potential would extend in to the probe. Obviously, ionization distances even as large as 100 m have a very pronounced effect on the magnitude of the probe potential to infinity. It also affects the shape of the potential curve throughout the sheath region, and especially close to the probe. Thus, if the technique for determining the probe potential experimentally only measures the differential potential between the probe and a point in space a few meters away, this measured differential potential might be only a small fraction of the probe potential to infinity.

It is fairly clear why the potential approaches a constant value equal to the ionization threshold energy at relatively small values of λ . The incoming electrons will create electron-ion pairs more or less uniformly throughout the volume near the probe where the local potential is greater than the threshold energy. The electric field in this region will accelerate the electrons toward the probe and the ions away from the probe. The electric field that results from this separation of the negative and positive charges will decrease the electric field that had existed before the separation. For large λ and small beam currents, the density of the electron-ion pairs will be small and the reduction which they produce in the electric fields, and therefore the probe potential, will be small. Conversely, for small λ and large currents, the electric field produced by the electron-ion pairs can almost completely cancel the previously existing field. Of course, the field cannot become negative in steady state because the electrons must always be attracted

toward the probe. In the limit of very high ionization density, the electric field must be just sufficient to remove the electrons from the ionization region at the same rate that the ions are removed, primarily by their assumed sweepout velocity, v_s . Only a fraction of an electronvolt potential difference is required to produce an electron velocity equal to the assumed value of $v_s = 5000$ m/s. Hence, in that case, the potential curve in the ionization region will be very flat and close to the ionization threshold energy.

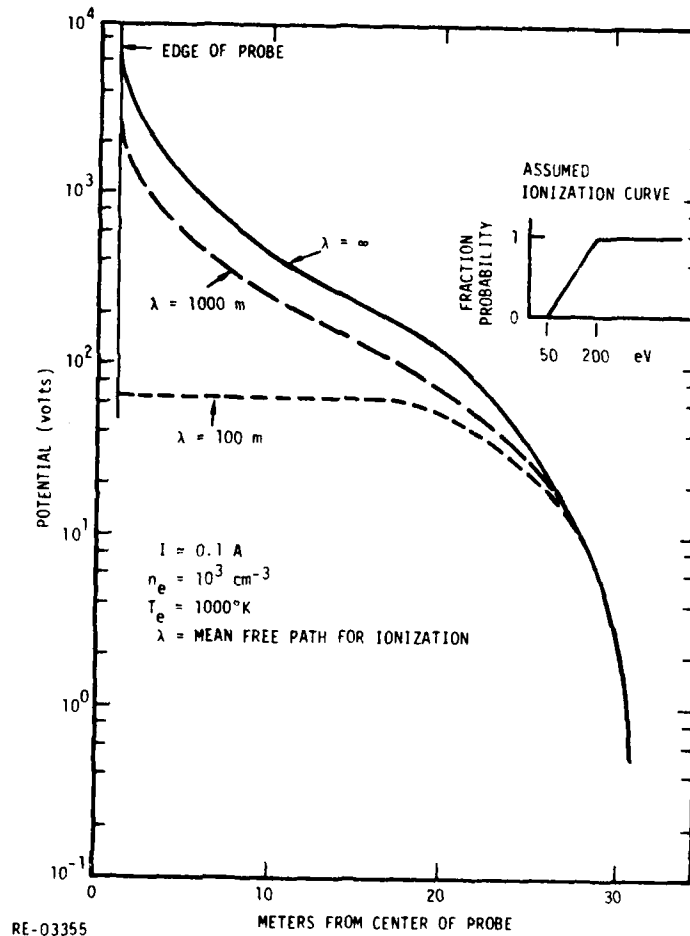
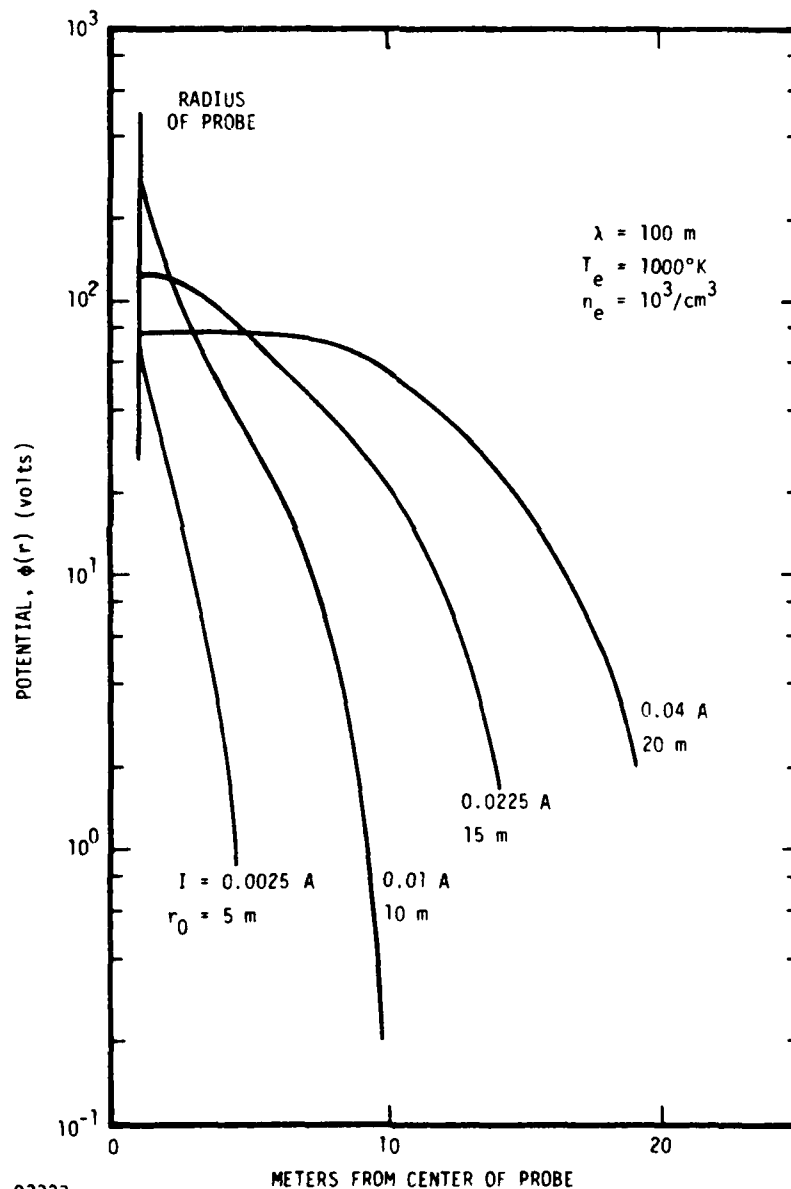


Figure 11. Radial variation of potential for different ionization rates

Figure 12 shows similar potential curves for different emission currents. The interesting point from this figure is that the probe potential to infinity actually goes through a maximum as a function of the emission current. This maximum is illustrated in Figure 13, where the potentials at the probe in Figure 12 are plotted versus the emission

current. At small values of current, the probe potential is less than the assumed ionization threshold (40 eV), so there is no ionization and the calculated probe potentials agree with the Langmuir-Child prediction. Perhaps just as significant, the differential potential between the probe and a point a few meters from the probe is much larger at a current of 0.01 A than it is at currents of 0.04 A and above.



RE-03333

Figure 12. Potential profiles for different emission currents

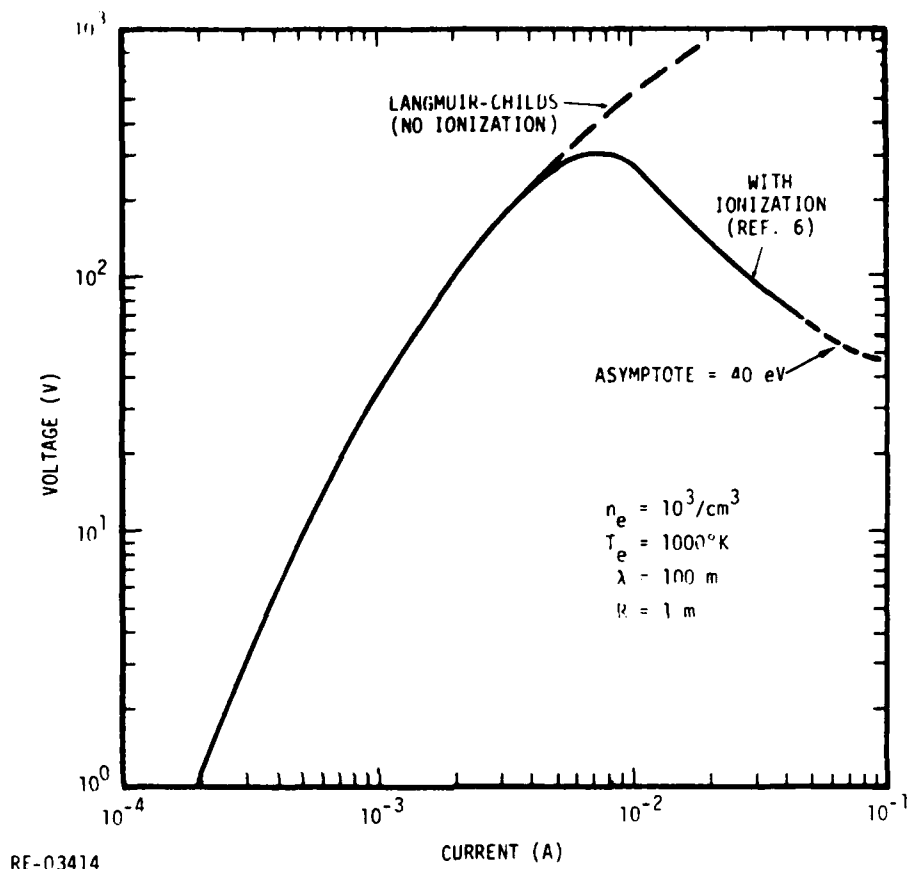


Figure 13. Probe potential versus beam current

The reason for the peak in the I-V curve is not as clear as the reason for the plateau in the potential curve. However, a plausibility argument can be developed by considering the curves in Figure 12. For a current of about 0.003 A, the probe potential is about 100 V, which is well above the ionization threshold. However, the radial distance over which the potential exceeds the ionization threshold is fairly small and not many ionization events occur in that distance. On the other hand, when the current is over an order of magnitude larger (≈ 0.04 A), the potential reaches the ionization threshold about 10 m from the probe. Hence, there is a long distance over which ionization will occur and there is over an order of magnitude more returning electrons to create the ionization. This abundance of secondary electrons causes the potential to remain closer to the ionization threshold, that is, less than the potential at a smaller current. It is interesting that the peak in the I-V curve will probably be less pronounced for very large

vehicles. For example, from Figure 12, if the probe radius had been, say, 10 m, essentially the same potential curves outside that radius would occur for the same currents. Although other curves at higher currents are needed to prove the point conclusively, it appears that the maximum potential for a 10 m-radius sphere might be only about 60 V.

Although it is unclear what densities of neutral atoms, and therefore λ 's, should be associated with the data points in Table 1, the calculated probe potential in Figures 11 and 12 for λ 's on the order of 100 m or less are in much better agreement with measured probe potentials for electron emission than are the predictions such as those in Table 3, which do not include ionization.

3.5 ORBITAL LIMITING

At this time, a brief discussion of orbital limiting is useful.

Consider a particle with mass and charge q , which has a velocity v_0 in a region where the electrostatic potential ϕ is zero. If this particle is attracted by a central force field toward a probe with radius R , it will strike the probe if its initial impact parameter is less than

$$p = R \left(1 - \frac{2q \phi_{\infty}}{mv_0^2} \right)^{1/2}, \quad (3-21)$$

where ϕ_{∞} is the probe potential relative to infinity (Ref. 5). Note that ϕ_{∞} is positive if the attracted charge q is negative. If its impact parameter is greater than p , the particle will miss the probe and continue on its path about the probe.

If we identify $(1/2 m v_0^2)$ with the thermal energy of electrons at infinity ($kT = 0.086$ eV for the problems in Section 3.4) and assume a probe potential of, say, 200 V, and $R = 1$ m, the critical impact parameter p is 48 m. By comparison, the outer radius of the sheath r_0 for an emission current of 0.1 A is 31.8 m for the plasma conditions used in Section 3.4. Thus, every particle at r_0 that has a component of its velocity directed toward the probe has an impact parameter smaller than $p = 48$ m and would be captured by the probe. Consequently, using the free-fall approximation for the electron velocities (Eqs. 3-18 and 3-19) appears justified for such a potential.

From Figures 11 and 12, the probe potentials with very high ionization might be as low as 40 eV. If we use this potential in Eq. 3-21 instead of the 200 V assumed above, the critical impact parameter would be only 18.5 m. This would indicate that the free-fall approximation would be inaccurate for emission currents greater than about 0.035 A ($r_0 >$

18.5 m). However, when there is a large amount of ionization, a more realistic criterion for the critical impact parameter might be to use an effective probe radius R in Eq. 3-21 equal to the location of the knee in the potential curve -- about 15 to 20 m for $I = 0.1$ A (Figure 11). Obviously, this approach would produce an extremely large allowable impact parameter. The rationale for this criterion is that the incoming electrons start to produce electron-ion pairs when they reach the ionization threshold, that is, at the knee in the potential curve. These ionization electrons are created with very small initial velocities and all of them are eventually captured by the probe. They can supply the difference in the return current to the probe with only a negligible change in potential if all of the primary electrons strike the probe in one case or if some of them miss the probe and orbit about it in another case. Hence, even if some orbit limiting does occur, it will have only a minor effect on the probe potential when there is high ionization.

A more rigorous discussion of orbital limiting should consider a Maxwellian distribution of the initial plasma electrons, as was done in Reference 5. On page 130 of Reference 5, it is shown that the current collected by a spherical probe with no ionization is very nearly the thermal electron current that crosses the sheath boundary at $r = r_0$ whenever

$$\exp \left[\left(\frac{-R^2}{r_0^2 - R^2} \right) \right] q \phi_\infty / kT$$

is small compared to unity. This quantity is the exponential $e^{-\phi}$ in Equation 45 of Reference 5. For $\phi_\infty = 200$ V, $r_0 = 31.8$ m, and $T = 1000^\circ\text{K}$, the magnitude of the above exponential is about 0.1, so the criterion is reasonably well satisfied. Actually, with no ionization and this current, ϕ_∞ would be much greater than 200 V, so the criterion would be satisfied even better. With ionization, the effective radius R of the probe should be increased, for the reasons discussed previously. This would make the absolute magnitude of the argument of the exponential larger, even for $\phi_\infty \approx 50$ V, so the exponential would be less than 0.1.

In summary, for the range of parameters used thus far in the computer model, and probably for the major range of interest, orbital limiting appears to be an insignificant effect, and the free-fall approximation for the attracted electrons is well justified.

4. ABORC CALCULATIONS

This section describes calculations of electron-beam emissions performed self-consistently in 2-1/2 dimensions using the ABORC SGEMP computer code (Ref. 9). "Self-consistent" in this context means that electromagnetic fields can alter charged particle trajectories, thus affecting spatial currents and the fields themselves. Advantages of the numerical approach described here are the minimization of environmental assumptions, capability to meet multidimensional geometries, and ease of operation of a previously existing tool. The code employs a full description of negative and positive particles which can move self-consistently in electromagnetic fields obtained from finite-differenced Maxwell's equations, and computes the time evolution of fields and currents around the vehicle. This allows for effects of orbital limiting, space-charge limiting, and the geomagnetic field automatically in the simulations. The approach has many similarities to that of Rothwell, executed previously in one dimension (Ref. 10). A test problem compatible with both ABORC and Rothwell's code was executed at AFGL's direction and gave similar results, as discussed below.

Disadvantages of using particle-pushing codes such as ABORC are typically the large computer core and execution time required to obtain stability and statistical accuracy in certain parameter ranges of interests (Ref. 16), particularly late-time conditions. Therefore, the results obtained for the present problem with the computer code are limited to a small fraction of the relevant parameter space--in particular, relatively low plasma densities and large plasma temperatures, and to relatively early times in the complex evolution of the probe/beam/environment system. However, usage of the code elucidates complex behavior caused by geometry, space-charge-limiting, and magnetic field effects, which would be much more difficult to address with simpler analytic models. Also, relevant parameters for analytic models can be determined by exercising the particle model for variations in the parameters. Results can be employed in constructing other models capable of solving the entire parameter range of interest.

The remainder of this section describes the computer code and modifications added to simulate the background plasma and the earth's magnetic field. The rudiments of the model are described and exercised for simple cases. Predictions of the effects of geomagnetic field and background ionization on the probe response are presented for wide ranges

of beam currents. Finally, a discussion of results in terms of the available experimental data is given, and implications for future measurements of interest are considered. Some of the initial modeling and results leading to the calculations reported here are discussed in Reference 17.

4.1 DESCRIPTION OF THE STANDARD ABORC CODE

ABORC is designed to solve Maxwell's equations by direct-finite-differencing in generalized coordinates for axisymmetric geometries. Spatial current densities are obtained from finite "particles" of charge which are followed through the spatial mesh of zones. Each particle represents many negative or positive charges and is acted on by the local electric and magnetic fields during each time step. Emission of arbitrary energy, angular, spatial, and time distributions of currents can be specified. The calculational volume may contain either conductors or vacuum, with variable conductivity, permittivity, and permeability (σ , ϵ , μ).

Boundary conditions for the ABORC code require the specification of an outer, perfectly conducting cylinder. Free-space solutions can be obtained by moving the outer boundary out so that there are many plasma Debye lengths between the probe and the outer walls (Refs. 17-18). Finite conductivities can be specified representing imperfect conductors, and dielectric structures and high-permeability regions may be treated. Backscattering of electrons can be specified where charge is re-emitted from surfaces upon contact.

The code was typically dimensioned for 6,000 spatial zones which may vary in size. Up to 100 conducting regions for specification of bodies of revolution can be employed. Randomizing techniques were employed for electron emission distributions. As many as 8,000 particles were tracked during any given time step for as many time steps as desired. The code is written in FORTRAN, and typical computer times vary from 3 to 60 min on the CDC 7600 (or approximately 5 times longer on the CDC 6600).

4.2 MODIFICATIONS FOR THE PLASMA-PROBE CALCULATION

The plasma-probe calculations required additions to the standard code for specification of the ambient ionized plasma, the magnetic field, and ionization of the neutral particles by electrons. The modeling for these additions is described here, along with modifications permitting use of the system on the AFGL CDC-6600 computers.

The background plasma is modeled by a large number of negative macroparticles representing electrons, and stationary positive macroparticles representing ions. The positive macroparticles are a direct and computationally free result of the fact that the code basically creates a quasi-neutral plasma at time zero and then moves the electrons while the ions remain fixed. The initial energy distribution of the electrons is rectangular with midpoint temperature value T (interpreted loosely as the plasma temperature) and with a spread equal to T ; that is, the distribution extends from $T/2$ to $3T/2$ with a constant magnitude. The initial angular distribution is isotropic, and the number density, n , is constant, ignoring the steady-state sheath that actually develops around a spacecraft. This is a good approximation as long as the probe potential with the beam on is large compared to the plasma temperature, and therefore large compared to the probe potential before the beam is turned on. The plasma is constantly exiting and entering at the outer boundaries of the simulation volume. Assuming that the boundaries are far enough away from the probe, a constant flux of electrons (equal to $ne\bar{v}/2$, where \bar{v} is the average normal velocity) strikes the walls. The plasma loss is compensated by a constant inward emission of plasma particles from the outer boundary, corresponding to the thermal motion only.

The simplifying assumptions in the plasma description are thought to be justified for the present calculations. Ions move approximately 1/10 of a probe dimension in the first 10 μs calculated here, so a zero velocity for the ions introduces very little error. A similar argument applies to a zero assumed rocket velocity. The uniform energy distribution assumption has not been tested for accuracy in the present work, but it is not thought to introduce any significant error.

Effects of the geomagnetic field are modeled with the field along the axis of the cylindrical coordinate system due to rotational symmetry requirements in the code. The appropriate terms were included in the Maxwell's equations:

$$-\frac{\partial H_{\theta}}{\partial z} = J_r + \dot{D}_r,$$

$$\frac{\partial H_r}{\partial z} - \frac{\partial H_z}{\partial r} = J_{\theta} + \dot{D}_{\theta},$$

$$\frac{1}{r} \frac{\partial}{\partial r} (rH_{\theta}) - \frac{\partial H_r}{\partial \theta} = J_z + \dot{D}_z,$$

$$-\frac{\partial E_{\theta}}{\partial z} = \mu \dot{H}_r,$$

$$\frac{\partial E_r}{\partial z} - \frac{\partial E_z}{\partial r} = \mu \dot{H}_\theta ,$$

$$\frac{1}{r} \frac{\partial}{\partial r} (r E_\theta) = \mu \dot{H}_z ,$$

where each term which references E_θ , H_z , or H_r has been newly added for the effects of the geomagnetic field. The particle equations of motion become:

$$v_z^+ = v_z + \frac{q\Delta t}{m\gamma} (E_z + v_r B_\theta - v_\theta B_r) ,$$

$$v_r^+ = v_r + \frac{q\Delta t}{m\gamma} (E_r + v_\theta B_z - v_z B_\theta) ,$$

$$v_\theta^+ = v_\theta + \frac{q\Delta t}{m\gamma} (E_\theta + v_z B_r - v_r B_z) ,$$

$$\gamma^+ = \gamma + \frac{q\Delta t}{2mc^2} \{E_z (v_z^+ + v_z) + E_r (v_r^+ + v_r) + E_\theta (v_\theta^+ + v_\theta)\} ,$$

where the superscript + denotes values at the end of the time step, and the newly added terms in the equations which treat the geomagnetic effects are those referencing E_θ , B_z , and B_r . Also, the substitution $\vec{B} = \mu \vec{H}$ has been employed, where μ is the permeability of free space. More detail on the development and solution of these equations is given in Reference 9.

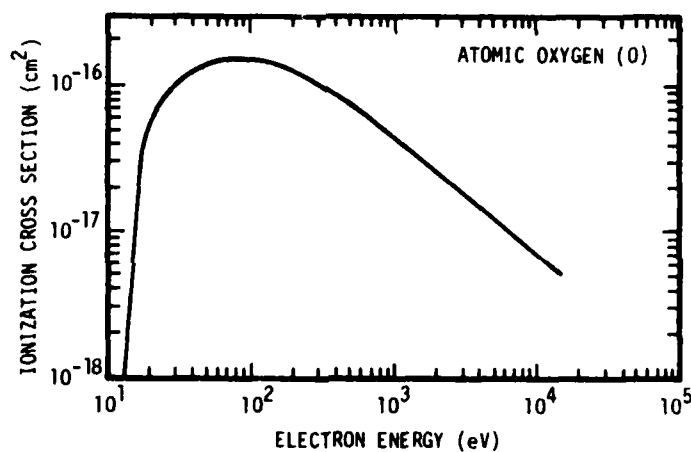
Simulations begin with a constant value for the geomagnetic field, B_{e_z} , everywhere in the grid at time zero. As particles gradually pick up a net azimuthal velocity, a magnetic field is generated in the opposite direction to B_e . The opposing field is, in general, spatially dependent. Hence, the particle motion and fields are calculated "self-consistently."

Ionization of neutral species is modeled using the cross section shown in Figure 14 (from Ref. 19). A single curve for atomic oxygen represents ionization by electrons of all species present in the ionosphere in the present model. The accuracy of the cross section is within a factor of 2 for the other species over most of the energy range, which is sufficient for the present model accuracy. In particular, the peak cross section for N_2 , which is the other dominant species at the altitudes of interest for sounding rockets, is about $2.5 \times 10^{-16} \text{ cm}^2$ and it also occurs around 100 eV. In the code, the oxygen cross section curve is approximated by a curve fit to Figure 14. The code emits new particles representing ionization products when the calculated charge buildup in a zone due to

ionization reaches some fraction of the ambient electron density. Specifically, a particle is emitted in a cell due to ionization when the following is true.

$$N \iint \frac{dn}{d\mathcal{E}} \sigma v d\mathcal{E} dt > fn ,$$

where f is an input parameter (typically set equal to 1), $dn/d\mathcal{E}$ is the energy spectrum of electrons in each zone, n is the total number, v is their velocity, and N is the neutral number density. The emitted electron is assumed to have 1 eV initial energy and random isotropic direction, and leaves behind a stationary ion.



RE-03026

- $N \int \frac{dn}{d\mathcal{E}} \sigma v d\mathcal{E}$ CALCULATED AT EACH SPATIAL POSITION FOR BEAM AND PLASMA ELECTRONS
- SECONDARY ELECTRON PARTICLES EMITTED FROM EACH CELL WHEN THE CHARGE DENSITY DUE TO IONIZATION BECOMES COMPARABLE TO INITIAL BACKGROUND ELECTRON DENSITY
- SECONDARIES EMITTED WITH 1-eV ENERGY
- COLLISIONAL ENERGY LOSS AND RANDOMIZING OF DIRECTION OF IONIZING PARTICLES NEGLECTED

Figure 14. Summary of treatment of ionization of neutral particles by electrons in the ABORC particle model for dynamic probe behavior

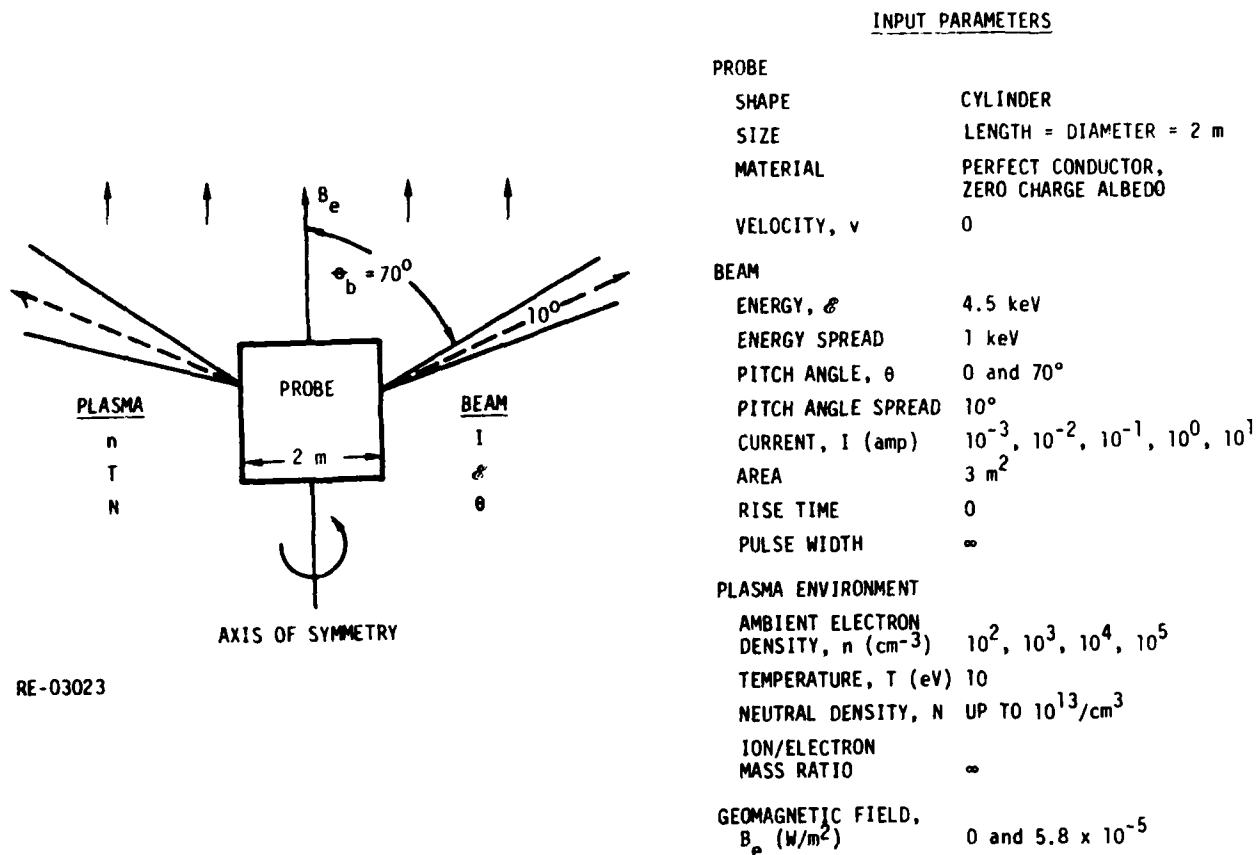
4.3 COMPUTER MODEL FOR THE PROBE, BEAM, AND PLASMA

The ABORC model for the probe, electron beam, and background plasma is illustrated in Figure 15. Major parameters defining problem components are listed on the right. The symbols are used in the remainder of this section to define problem input parameters. The probe has been considered to be a simple cylinder primarily for purposes of comparing initial results of the calculations with simpler spherical models. A more realistic rocket-shaped geometry could be treated by the code, and may behave somewhat differently in magnitude, but will probably show the same qualitative behavior as a function of major parameters. It is assumed that electrons which strike the probe are not re-emitted because secondary electrons generally have low energies (around 2 eV), so they would be immediately attracted back to the vehicle and thus produce negligible effects. However, a problem at higher plasma density or lower beam energy might require the inclusion of secondary electrons. Treating the vehicle as stationary should introduce minimal errors for cases where the ionization of background neutrals is neglected. The time scale to move an object dimension is much longer than the plasma frequency. A stationary ion model should be sufficient for the same reason.

Beam parameters define the energy, angular, spatial, and temporal characteristics assumed in the analyses. The values shown are intended to represent a recent experiment by Cohen (Ref. 2) within the ability of the computer model. In actuality, the beams are highly concentrated over a small area, are emitted at some angle to the geomagnetic field, and are confined to a smaller angular spread. In the code, the beam is assumed to be emitted over a much larger area to ensure that several finite-difference zones are overlapped by it. The rotational symmetry requirement allows a pencil beam along the coordinate system axis parallel to the geomagnetic field only. For emission at an angle to the field, the beam must necessarily fan out like a cone, as illustrated. This restriction introduces questionable geometry differences between the experiments and the analytical models, but it does not inhibit magnetic field effects on the beam transport. The beam angular spread is small in the code, as it is in the experiments. The pulse shape is a step function at time zero which accurately models the time interval treated by the code.

The pertinent plasma quantities are the initial electron-ion number densities and temperatures and the neutral species densities. The values shown are for the ranges considered in the present calculations. The 10-eV electron temperature is artificially high (1 eV is the physically reasonable upper limit), but it was employed in most cases as an economy measure during the development stages of the modeling. The positive ions have

been taken to be stationary during the early time evolution ($\sim 20 \mu s$) due to their relatively large mass. The computer code could treat them as mobile, but they were omitted for reasons of economy.



RE-03023

Figure 15. ABORC code model for a rocket-borne electron beam emission into a neutral plasma

Electric and magnetic field solutions were obtained by finite-differencing Maxwell's equations on a grid of 28 axial by 18 radial cells. The minimum size was 0.33 m near the vehicle, and increased smoothly to 1.6 m at the outer boundary. This grid permits approximately two cells per Debye length near the vehicle and is economical enough to allow solutions of the field equations over the long simulation times. The mesh size is slightly larger than the Debye length in the outer reaches of the volume, but it is thought that this will have little effect far from the object. The primary limitation to finite-differenced Maxwell's equations occurs when small zones are required. Then time steps

must be reduced and computer times may become excessive. The present simulation with a 0.74-m Debye length and non-space-charge-limited beam permits a reasonably economical calculation.

The background plasma is represented initially by typically 2400 particles representing the free electrons. Considering the volume of each particle (particles are actually annuli in two dimensions), we have approximately six per Debye volume near the vehicle. This number is adequate for the close-in representation of the plasma. We have employed considerably fewer particles per unit volume at larger distances from the object for economic reasons.

The initial condition of the satellite-plasma system was artificial in the simulations. In an actual experiment, an equilibrium would occur in which a sheath would exist about the vehicle. Our simplified initial condition, in which the vehicle instantaneously appears in the middle of a boundless, homogeneous medium and simultaneously begins emitting electrons, results in system adjustments both to the presence of the conducting object and to the fields caused by the energetic particles. The system is unaffected by this simplification after a few plasma periods, but the time evolution may be suspect at very early times.

Time scales for the simulation are determined by the Courant condition for fields, and by the minimum transit time across a Debye length for particles. In a typical case, the step sizes employed are 0.7 ns for fields and 20 ns for particles. Even with the resulting 30:1 time step ratio of particles to fields, the calculational cost is dominated by the particle position updating.

The following summary highlights the ABORC code particle model used for early-time dynamic probe behavior.

- Rotationally symmetric probe and beam modeled in 2-1/2 dimensions.
- Time-dependent Maxwell's equations solved self-consistently, including effects of space-charge limiting.
- Conducting outer boundary --

$$\phi_B = 0.$$

$J = nev/2$, where v is the inward component of the velocity from the initial energy distribution emitted isotropically.

- Lorentz force, including geomagnetic field acting on beam and plasma particles.

- Ionization of neutrals.
- Stationary ions.
- Electron albedo = 0.

4.4 CALCULATED BEHAVIOR OF THE PROBE FOR SIMPLE CONDITIONS

Figure 16 shows the time evolution of the probe potential for the simplified conditions of no geomagnetic field and no ionization of neutrals, for several assumed background electron densities. Notice that the background reduces the potential compared to the case with no plasma (the dashed line), and that the reduction is greater for greater electron densities. The plasma is able to provide replacement current through its thermal velocity more effectively for higher densities until, at the highest density value, the probe potential is essentially the same as the electron temperature. However, as pointed out in Section 4.2, the accuracy of the calculation becomes marginal when the probe potential is not significantly larger than the plasma temperature.

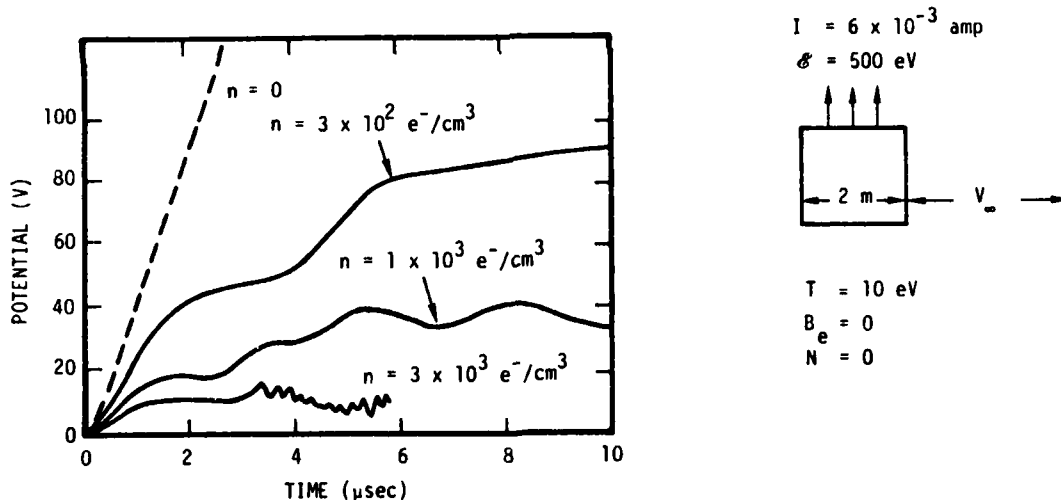


Figure 16. ABORC particle calculations for probe potential time evolution for different electron densities

The case with no background plasma shows potential increasing linearly with time, since no charge flows back to the probe to neutralize it. If the calculation had been extended to late times, the potential would have risen to the beam energy ($\sim 4.5 \text{ kV}$), and all further beam electrons leaving the probe would return.

A direct comparison between ABORC and Rothwell's code (Ref. 10) was made using the $10^3/\text{cm}^3$ density case of Figure 16 and a uniform emission from the surface of the ABORC model and no geomagnetic field to be consistent with the Rothwell model. The steady-state potentials from the two codes were within 2 or 3 V, and the oscillation periods were within 20%, which is excellent agreement. In addition to the different geometries between the ABORC and Rothwell models, there were several other differences such as somewhat different boundary conditions and the Rothwell model is quasi-static whereas ABORC is fully dynamic. The test problem calculations are described in more detail in Reference 17.

4.5 EFFECTS OF THE GEOMAGNETIC FIELD

When the earth's magnetic field is included in the calculations, it affects both the beam and plasma electrons (plasma ion motion perturbations due to the B-field are negligible because of large mass and low velocities). The effects are summarized in Figure 17. Beam electrons are bent into Larmour orbits (radius R_L) if they cross magnetic field lines. They can reach a maximum distance perpendicular to the field of $2R_L$, but can spiral to great distances from the probe along the flux lines. The effect is dependent on the magnitude of the beam current in that it becomes insignificant at large beam currents where the probe potential always approaches the beam energy. Plasma electrons are also constrained to move in tight orbits (equal to 0.2 m for the presently employed artificially high temperature of 10 eV). Since the electrons cannot cross field lines, return current comes from a tube equal approximately to the probe diameter. Higher probe potentials result from the smaller area of the plasma supplying return currents.

The increased probe potential due to the geomagnetic field is illustrated dramatically in Figure 18A for a low-current electron beam emission parallel to the field. The lower two graphs in the figure are the total electron currents returning to the side and bottom (Figures 18B and 18C) of the probe due to the plasma. Although it is not shown, an amount of current comparable to that on the bottom of the cylinder returns to the probe on the top of the cylinder. The current striking the bottom is only moderately affected by inclusion of the earth's field, B_e , because electrons move parallel to it in striking that surface. Current returning to the side is dramatically reduced, however, because the low-energy plasma electrons cannot cross the field lines. The effect on the probe potential is to cause it to increase substantially over the case without B_e (upper figure) because the plasma cannot provide return current fast enough to hold it down. This effect,

demonstrated here numerically, was predicted analytically in 1967 by Parker (Ref. 6). It is interesting that the sum of the quasi-steady current to the side of the cylinder with $B_e = 0$ (≈ 4 mA), the relative current to the bottom of the cylinder (≈ 1 mA), and an additional estimated 1 mA to the top of the cylinder equals the emission current (6 mA), as it should in quasi-steady state.

EFFECTS ON BEAM

- NO EFFECT FOR EMISSION PARALLEL TO B_e
- LIMITED TO $2R_L$ (≈ 8 m) RADIAL DISTANCE FROM PROBE FOR 70° PITCH ANGLE
- BEAM CURRENT LEVEL DEPENDENCE

EFFECTS ON PLASMA

- RESTRICTS RADIAL MOTION OF ELECTRONS ($R_L < 0.2$ m)
- $\vec{E} \times \vec{B}$ DRIFT CAUSES J_ϕ
- MOST RETURN CHARGE FROM REGIONS IN DIRECTION PARALLEL TO \vec{B}
- HIGHER PROBE POTENTIALS
- EFFECT NOT STRONGLY DEPENDENT ON BEAM CURRENT LEVEL

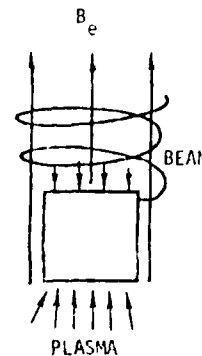


Figure 17. Effects of earth's magnetic field

Figure 19 shows the effect of the geomagnetic field on probe potential for a wide range of electron beam currents. The probe potential was computed with and without the field, B_e , for a low-density plasma. The results plotted are the maximum values observed during the first $15 \mu s$ of the simulation. The potential which would have been achieved at $15 \mu s$ in the absence of a background plasma is also plotted. This latter potential would continue to increase until it reached the beam energy. The presence of B_e increases the potential when there is a plasma by about an order of magnitude at the smaller currents. Note that the potential finally reaches the beam energy (≈ 5 keV) with or without the magnetic field for high current conditions due to the dominance of the electric field limiting of the beam particles.

The effect of the geomagnetic field on probe potential was also considered for different beam pitch angles. The beam was emitted parallel to the field (0° pitch) and almost perpendicular to it (70° pitch), as illustrated in Figure 20. The beam was restricted to an 8-m radial distance from the probe in the latter case, but it spiraled upward unrestricted. The final probe potential was found to be the same in either case for a low

beam current ($\sim 10^{-2}$ A) with a 5-keV beam. Effects of the pitch angle may be slightly greater at high beam currents, but the parameter does not appear to be significant with regard to interpreting probe potentials based on this simulation.

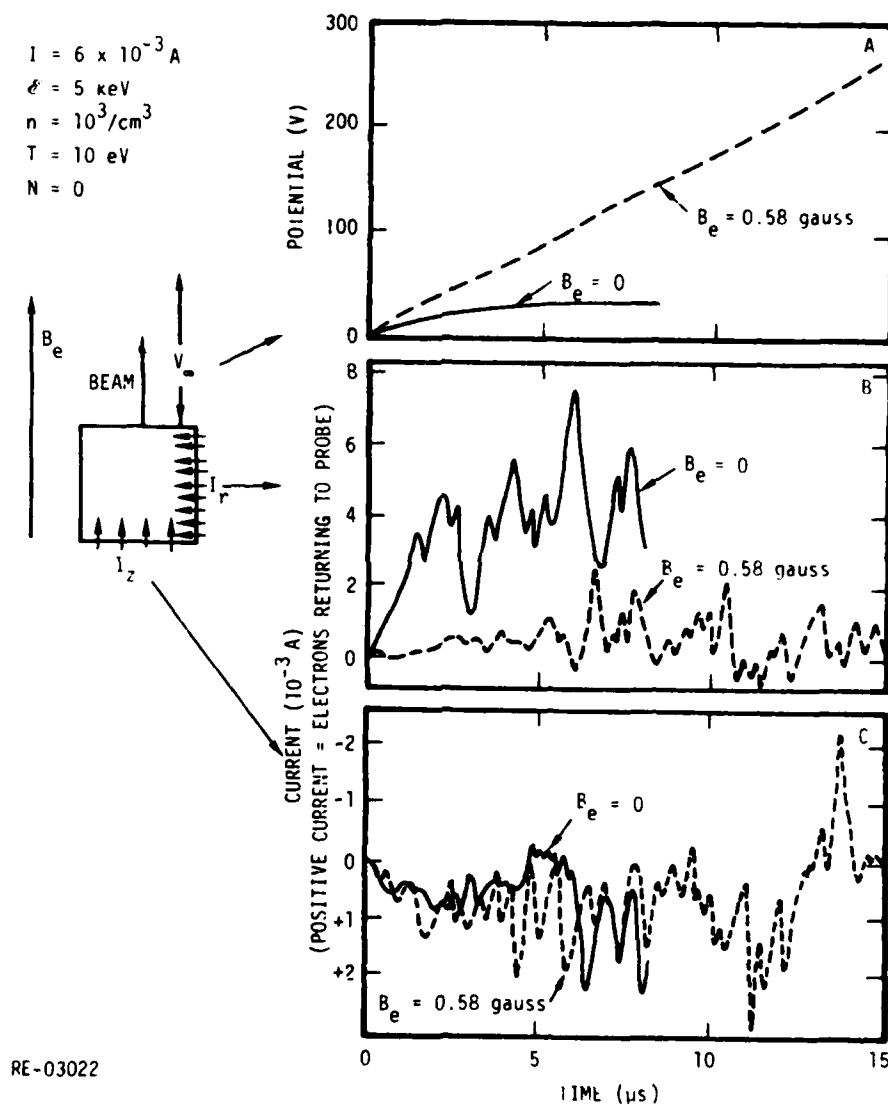
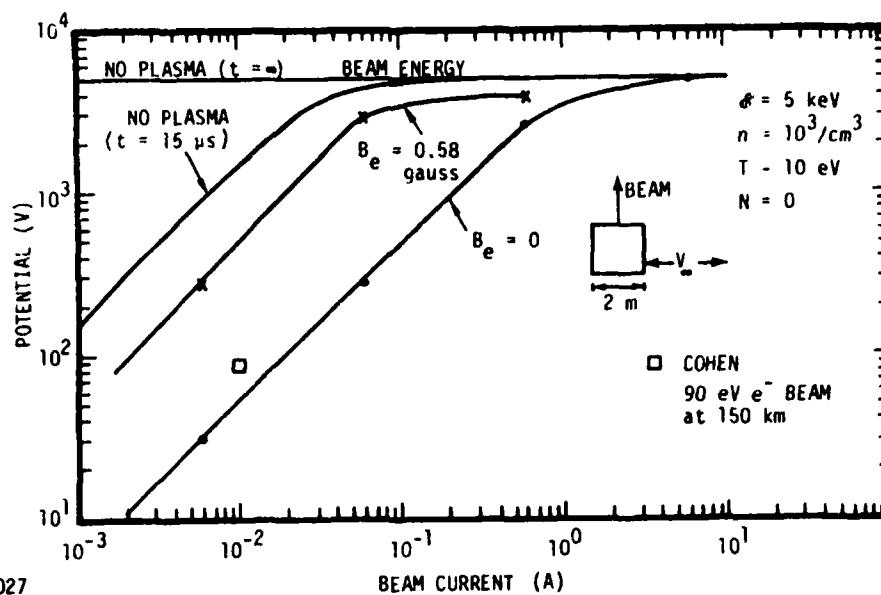
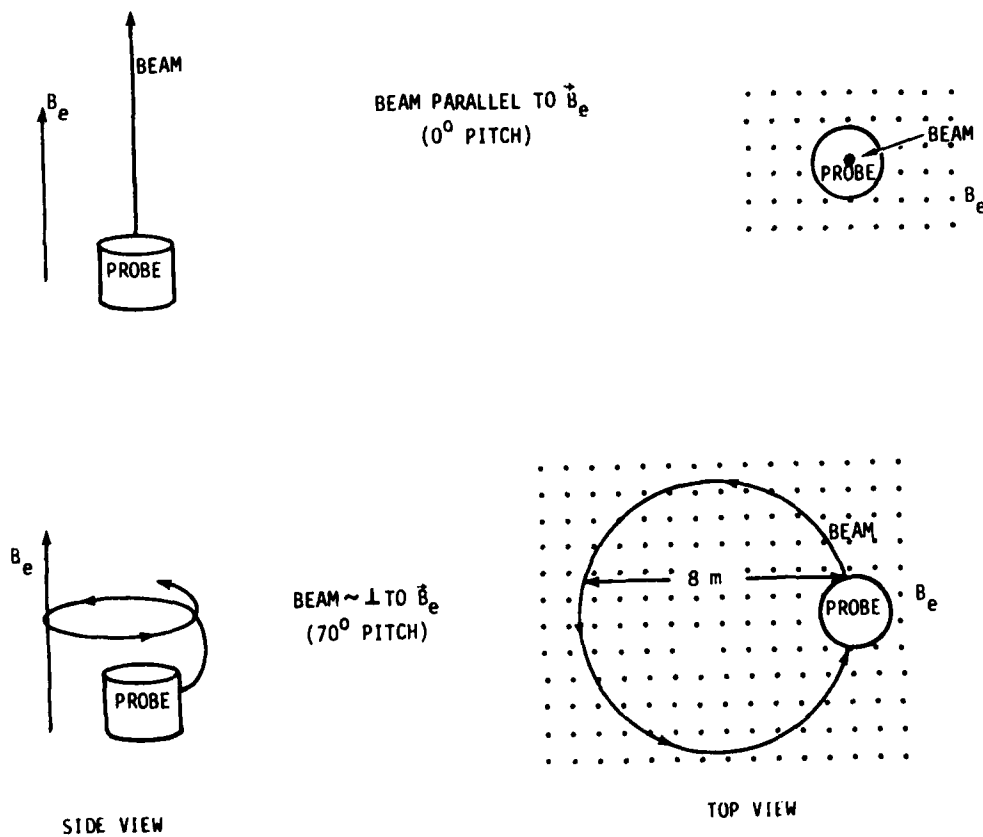


Figure 18. Probe potential and plasma return currents calculated with and without the geomagnetic field



RE-03027

Figure 19. Maximum probe potential during the first 15 μs calculated with and without the earth's magnetic field using the ABORC code particle model



RE-03025

Figure 20. Illustration of effects of beam pitch angle on system behavior

Effects of the geomagnetic field on the early-time plasma-probe behavior are summarized below.

- B-field hinders plasma motion perpendicular to field lines.
- Probe potential increases as much as 10 times over value obtained without B-field modeled.
- Effect on probe potential is significant at all but highest beam current levels.
- B-field reduces effective collection area of probe, suggesting a potential dependence on probe area normal to field lines.
- Probe potential is not dependent on beam pitch angle.

The field hinders plasma current returning to the vehicle, causing vastly greater electric fields than would otherwise occur. The effects of the geomagnetic field require modeling for all but the highly space-charge-limited beam currents to accurately predict the potential. This behavior suggests that an interesting experiment would be to measure the time-dependent potential of a rocket with the major axis first parallel and then perpendicular to the field lines. The small area normal to the geomagnetic field would presumably result in a potential that is much greater than in the orientation with the large area normal to the field for the same beam emission current. The calculations showed that the potential was not strongly dependent on the beam pitch angle to the magnetic field.

4.6 EFFECTS OF IONIZATION OF NEUTRALS ON EARLY-TIME BEHAVIOR

Inclusion of ionization of the neutral particles in the background environment allows beam and plasma electrons to create additional electrons and positive ions through collisions. Effects increase with increasing neutral density in this regime, and with decreasing beam energy. The degree of ionization will be dependent on the magnitude of the beam current in that the beam current affects the probe potential and the energy of the returning electrons, and thus the average ionization cross section of the electrons. The effect of ionization in general is to reduce the probe potential by increasing the supply of electrons available to allow replacement of the beam charge at lower field levels.

Background ionization effects are shown in Figure 21, where the probe potential to infinity is compared with and without a high-density neutral species present. Notice that

the potential is approaching the beam energy ($\mathcal{E} = 5$ keV) in the case without the background species, and that it reaches only ~ 1 kV with ionization. The time at which ionization effects become observable on the graph (~ 1 μ s) corresponds well with the "dissipation time," $\tau_{\text{dis}} = 1/N\sigma v$, where σ is the cross section corresponding to electrons of velocity v which ionize the neutral background species of density N . τ_{dis} is the time required to produce ionization charge equal to the initial ambient value, n . The values for τ_{dis} can be as low as 0.7 μ s for the present conditions, if the ionizing particles are in the 100-eV region. This energy is no doubt prominent in the plasma distribution for the exhibited probe potential. Incoming electrons are accelerated into this energy range and efficiently reproduce themselves through ionization.

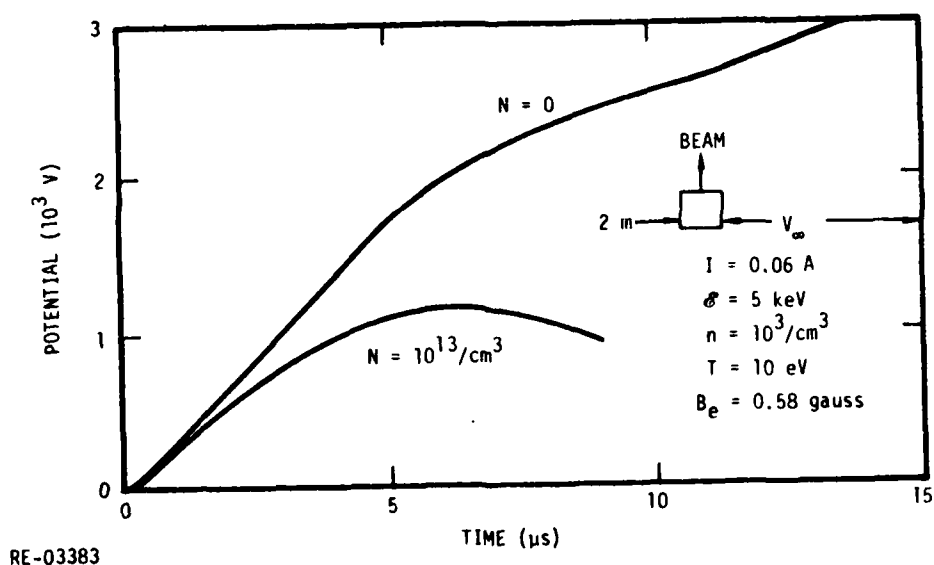


Figure 21. Probe potential calculated with and without ionization of a neutral background species

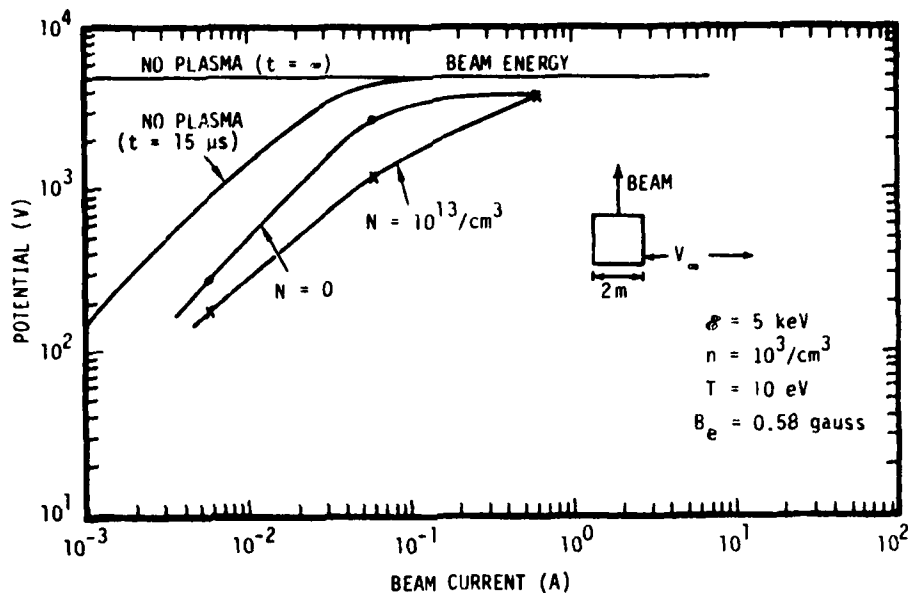
Unfortunately, the calculation had to be stopped shortly after the peak potential was achieved due to computer costs. However, notice in Figure 21 that the potential is still falling at 9 μ s. It might have converged to a steady-state value much closer to the value typically observed, 100 V, if it had been carried to later times.

The importance of ionization on the early-time probe behavior was quantified over a wide range of beam currents by computing the potential with and without ionization of the neutral particles included. Both sets of calculations included the geomagnetic field treatment, and the ionization case was done for the estimated maximum neutral-particle density of 10^{13} neutrals/cm³. Only moderate (< factor of 3) decrease in the peak probe potential was computed due to ionization for the conditions shown in Figure 22 during the 15 μ s of the simulations. The minimum mean free path for ionizing collisions in the calculations was ~ 6 m, and so the lack of effect for early times is not unexpected since typical electrons travel at most a couple of mean ionization lengths in the simulation time (≈ 9 μ s), so not many ionization events occur. Late-time (\sim ms) effects can still be significant, however (see Section 3).

The effects of the ionization of neutrals on early-time probe behavior are summarized below for a low-density ambient environment ($n = 10^3$ /cm³).

- Ionization by primary electron-beam particles is negligible.
- Acceleration of plasma electrons to energy >15 eV causes beam-current-magnitude-dependent ionization of neutrals.
- For a 5-keV beam and low-ambient-density electron environment, maximum effect is seen at beam current magnitude of 0.06 A.
- Peak potential is reduced to as little as 40% of value computed without ionization for a neutral density corresponding to the highest value in the altitude range of interest.
- Effect on probe potential diminishes as beam current is increased beyond 0.06 A as the probe potential approaches the beam energy. For a larger beam energy, the largest effect of the ionization would probably occur at a larger beam current.
- Effects may be larger at higher ambient electron densities.

In Figure 22, the curve for $N = 10^{13}$ /cm³ is less steep than the curve for $N = 0$, until the potentials approach the beam energy. Thus the effect of ionization apparently increases with increasing beam current. Based on the steady-state results in Section 3, this dependence probably occurs because the region over which the potential in space exceeds the ionization threshold is larger at larger currents. Consequently, there is more volume in which ionization can occur, and thus ionization should have a larger effect on the probe potentials.



RE-03028

Figure 22. Early-time peak probe potential calculated with the ABORC particle model with and without secondary-electron production due to ionization of neutral species. The value plotted is the maximum value observed during the first 15 μ s of beam emission.

4.7 SUGGESTED EXPERIMENTAL MEASUREMENTS BASED ON CALCULATED EARLY-TIME PLASMA/PROBE BEHAVIOR

Results of the ABORC code calculations of the early-time behavior of the probe are not directly comparable to available experimental data because the experimental data are for essentially the steady-state late-time regime. However, the differences between the predicted early-time and measured late-time results suggests some additional experimental measurements.

The probe potential was tending toward measured low values when the calculations were stopped, after having shown potentials generally much greater than the values measured experimentally on a 1-ms time scale (Figure 21). For example, a beam current of 0.8 A resulted in a 3-kV peak probe potential with ABORC compared to experimentally measured values of 3 to 30 V (see PRECEDE results in Table 1). The slight differences in beam energy between experiment and calculation would not account for any major discrepancy in the results. An interesting measurement then would be to obtain the peak probe potential as well as its "steady-state" value. Then it would be significant to see if

the peak value is sensitive to the rocket area normal to the geomagnetic field, and if the steady-state value is not. A rationale for the measurements is that the early-time potential is strongly dependent on geomagnetic field effects which may be dependent on the rocket orientation, whereas the steady-state value is driven largely by the ionization cross section.

5. SUMMARY OF RESULTS

The following are the main conclusions from this study.

1. For small magnitudes of the beam current, the steady state potentials of an ion- or electron-emitting probe in a partially ionized plasma can be predicted fairly well using one-dimensional spherical models without ionization of the neutral background particles.
2. For large ambient plasma densities, where the Debye length is small compared to the vehicle dimensions, care must be used in choosing the effective spherical radius of the probe for making the estimates.
3. For electron-emitting probes, when the probe potential exceeds the threshold for ionization of the neutral background gas and the mean ionization distance by electrons is less than about 200 m, it is important to include in the predictions the effect of ionization of neutral particles by the electrons which return to the probe to replace the beam current.
4. The I-V curve for an electron-emitting probe when ionization is important apparently goes through a maximum. At very large electron-beam currents, the probe potential asymptotically approaches the ionization threshold energy.
5. When ionization of the neutral background gas is important, the spatial variation of the potential curve in the region around the probe will be quite flat for considerable distances away from the probe. Thus, a measurement of the differential potential from the probe to some nearby point in space could be considerably less than the potential of the probe to the ambient plasma.
6. At early times after the emission beam has been turned on, the probe can rise to a potential that is considerably larger than the late-time potential if ionization of the neutral gas is significant.
7. The presence of the earth's magnetic field (B_e) increases the probe potential relative to what it would be in the absence of B_e . The magnitude of this change is dependent on the beam energy, the beam current, the densities of the ambient plasma and the

neutral particles, and probably the orientation of the probe geometry relative to the direction of the magnetic field. However, the orientation angle of the emission beam relative to the direction of the magnetic field has little effect on the probe potential.

APPENDIX A

TWO-FLUID PLASMA CODE

A.1 INTRODUCTION

This appendix describes an alternative approach that might be used in future calculations of plasma probe problems. The idea for this approach arose late in the present program when the difficulties of simulating late-time effects with particle-pushing codes became apparent. A small amount of work and code development were performed on this approach during this program, and a few preliminary results were obtained. However, the program came to an end before the code could be fully developed and checked out for the conditions appropriate to realistic probe environments. Hence, this appendix just summarizes the major ideas for the approach and the status of the code.

This two-fluid plasma code is a modification of a previously existing code, PRECHG, to consider the plasma electrons and positive ions as two independent, charged, compressible fluids. The original PRECHG code was basically a Poisson's solver which calculates the potential on an r - z mesh grid in a cylindrically symmetric geometry for an arbitrary distribution of charge in the radial (r) and axial (z) directions. That code starts by moving charge from one point in the geometry to another along r or z mesh lines, leaving behind a compensating amount of charge of opposite sign on the original sites. To conserve electric flux, an initial electric field is specified along these mesh lines, corresponding to the amount of charge that was transported along them. Although this initial distribution of charge conserves electric flux, it normally would not satisfy Poisson's equation because $\nabla \times E$ would not be zero everywhere in the volume. The code then iterates a series of equations alternately in the r and z mesh rows, which tend to reduce $\nabla \times E$ to zero everywhere in the volume of interest. The iteration is terminated when the maximum absolute value of $\nabla \times E$ at any mesh location is below some prespecified magnitude.

When the code is modified for a two-species plasma, the net current flow (ions minus electrons) along each mesh line at the beginning of a time step is used to calculate a change in the electric field along those mesh lines. Again, these electric fields normally do not correspond to $\nabla \times E = 0$ everywhere in the volume, so the code iterates the fields

after each time step to bring $\nabla \times E$ back within acceptable limits. The change in electron and ion densities at each mesh point is then calculated from the continuity equation. Finally, these carrier densities and electric fields are used to calculate new current densities for the start of the next time step, and the process is repeated.

Since the above procedure solves only Poisson's equation and not Maxwell's, the results are necessarily quasi-static but still time-dependent. Fortunately, for many situations the frequencies of interest are low enough that a quasi-static solution is quite adequate.

The main uncertainty in the problem, as discussed later, is the proper physics to put into the code to generate the local current densities (as functions of the densities and electric fields or potentials) for the carrier species that is attracted to the probe and the one that is repelled from the probe.

The first assumption that was used corresponded to both species being in quasi-equilibrium, corresponding to the local potential at every position in space. This assumption is appropriate for relatively high densities of the charged or neutral particles, such that mobility-limited flow is applicable. The resulting equations are identical in form to the equations for electrons and holes in semiconductors. The present authors have had extensive experience in programming and solving these equations for semiconductors, which was readily adaptable to the plasma problem. This model gave very encouraging comparisons to the analysis of Reference 10 for a non-emitting probe, where the resulting probe potentials were not very large, even though the analytic model in Reference 10 employed the orbit-limiting effect for the attracted (ion) species. However, it was recognized that, for lower plasma densities and high emission currents (large probe potentials), the quasi-equilibrium approximation for the attracted species could be significantly in error. The "free-fall" approximation for the attracted species is more suitable for those conditions. Under this assumption, the velocity of the attracted species in steady state is determined uniquely by the local electrostatic potential relative to the background plasma. Unfortunately, the present program came to an end before the physics corresponding to this free-fall approximation could be fully incorporated and checked out in the code. However, preliminary results indicate that there will apparently be no fundamental difficulties in solving the problem using this approximation.

A.2 MESH GEOMETRY

The mesh geometry for this code is illustrated in Figure 23. A body (conducting or

dielectric) of arbitrary r - z dimensions is enclosed inside an outer conducting cylinder. This type of system is often called 2-1/2 dimensions because bodies of finite size, similar in shape to real space vehicles, can be simulated. If the outer cylinder is located more than a couple of sheath thicknesses from the inner body, it will have no significant effect on the solution to the problem.

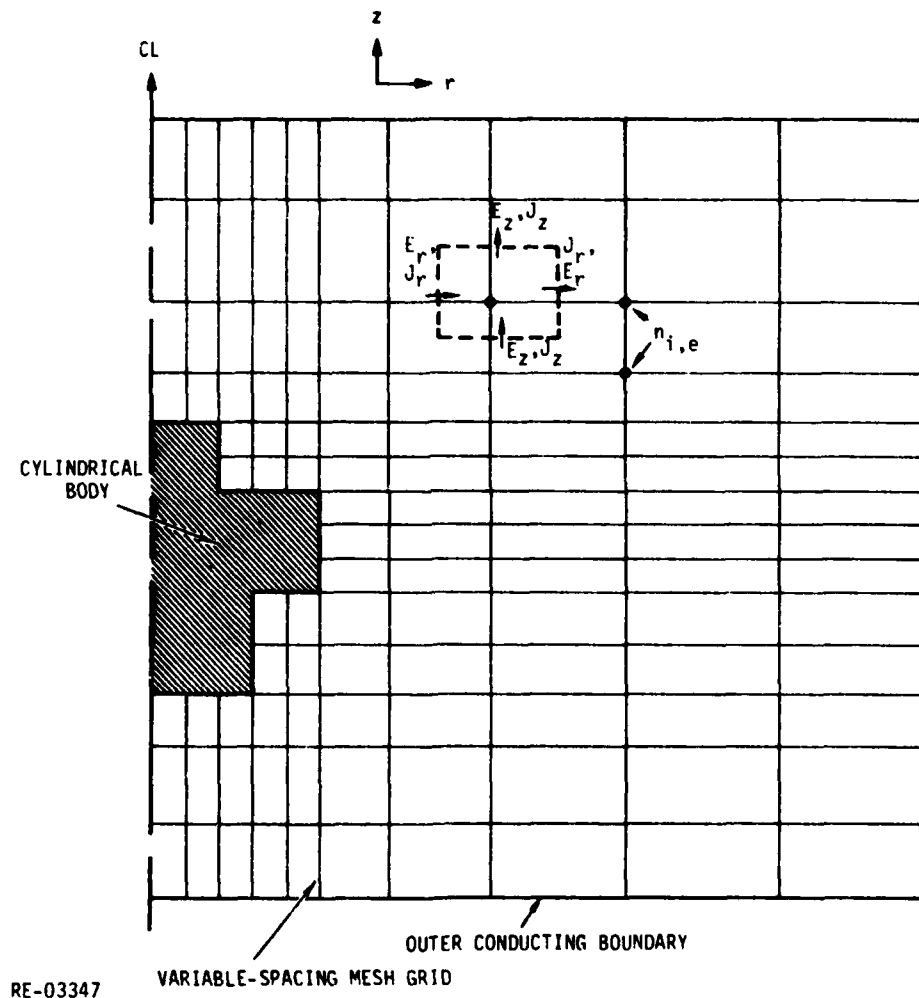


Figure 23. Mesh geometry for code (see discussion in Section A.2)

Carrier densities are defined at the intersections of the mesh lines and, therefore, on the boundary of the outer cylinder and the body. These densities are essentially assumed

uniform over the rectangular regions around each mesh intersection illustrated by the dashed lines in Figure 23. Electric fields and current densities are defined along the mesh lines but at locations midway between the mesh intersections -- that is, midway between the carrier densities. In this system, the continuity equation expresses the rate of change of the average density inside one of the dashed rectangles in the figure due to the net current that crosses its four boundaries. Similarly, Poisson's equation requires that the net electric flux leaving one of these rectangles must correspond to the net charge (ions and electrons) inside the rectangle. The requirement that $\nabla \times E = 0$ is rigorously equivalent to requiring that the line integral of the electric field around any enclosed area defined by mesh lines (solid lines in Figure 23) should be zero.

A.3 PLASMA EQUATIONS

The basic equations for this code involve:

1. Particle current densities, $J_{e,i}$, for each species between adjacent mesh intersections (e = electrons, i = ions).
2. Continuity equations for each species at each mesh intersection,

$$\dot{n}_{e,i} = \nabla \cdot J_{e,i} , \quad (A-1)$$

where n is the average carrier density in a mesh region.

3. Time rate of change of electric field between adjacent mesh intersections due to current densities, before adjusting $\nabla \times E$ toward zero (essentially a one-dimensional Poisson's equation),

$$\dot{E} = (-q_i J_i - q_e J_e) / \epsilon_0 , \quad (A-2)$$

where ϵ_0 is the permittivity of free space and q_i and q_e are the charges on the ions and electrons, respectively ($q_i = +$, $q_e = -$). When q is used without a subscript, it denotes the absolute value of the electronic charge.

4. $\nabla \times E$ iteration to reduce the curls to essentially zero.

A.3.1 Current Equation for Repelled Species

In the literature on charged-particle probes, it is generally assumed that the plasma species that is repelled from the probe is essentially in thermal equilibrium with a Maxwellian energy distribution at every point in space (Ref. 5). If the species is actually

in equilibrium (no currents and/or rates of change of density), the particle density at any place in space is given by the equation

$$n(x) = n_0 \exp[+q\phi(x)/kT] , \quad (A-3)$$

where n_0 is the particle density for that species in the plasma far from the probe where ϕ is zero, $\phi(x)$ is the electrostatic potential at position x (relative to zero at infinity) = $-\int_0^\infty E(r)dr$, T is the Maxwellian temperature which characterizes the particular species, and k is Boltzman's constant.

If there are any currents of the repelled species in the plasma, either steady-state or transient, Eq. A-3 is not rigorously satisfied. However, it is fairly close to correct and can be used to develop an equation for an effective particle current density (I) in terms of the gradients of the particle density and the potential.

Consider a very simple system that has only two equal-size mesh zones, as illustrated in Figure 24, with densities $n_{1,2}$ defined at points 1 and 2 along with the corresponding electrostatic potentials $\phi_{1,2}$. When the particles are in nearly thermal equilibrium at each point, the velocities of the particles with densities n_1 and n_2 are distributed isotropically with Maxwellian distributions. Therefore, half of the particles at n_1 will be moving toward n_2 with an average velocity in the positive x direction given by

$$v_{Tx} = \int_0^\infty v_x \left(\frac{m}{2\pi kT}\right)^{1/2} \exp(-mv_x^2/kT) dv_x = \sqrt{\frac{2kT}{\pi m}} , \quad (A-4)$$

where m is the mass of the particles (Ref. 5). Similarly, half of the particles at n_2 will be moving toward n_1 with the same average velocity v_{Tx} . However, due to the potentials ϕ_1 and ϕ_2 , the Maxwellian distributions are skewed in the direction of the electric field (x direction in the present problem). The differences in the potentials at points 1 and 2 from the value at the midpoint between 1 and 2 are $\pm E \Delta x/2$. Therefore, if the potential in the exponential in Eq. A-4 is adjusted for the electrostatic potentials at points 1 and 2, the average velocity of the particles in one region toward the other region is

$$v_{x1} = v_{Tx} \exp(qE \Delta x/kT)$$

and

$$v_{x2} = v_{Tx} \exp(-qE \Delta x/kt) . \quad (A-5)$$

The rates of change of the densities n_1 and n_2 in this two-zone system are then

$$\dot{n}_1 = \frac{-1}{\Delta x} \left(\frac{n_1}{2} v_{x1} - \frac{n_2}{2} v_{x2} \right), \quad (\text{A-6})$$

$$\dot{n}_2 = -\dot{n}_1. \quad (\text{A-7})$$

Expanding n_1 and n_2 about their average value [$n_{\text{ave}} = 1/2(n_1 + n_2)$] and the exponentials in Eq. A-5 up to first-order terms, and dropping the higher-order products of $\Delta n = n_1 - n_2$ and $qE \Delta x/kT$, Eq. A-6 becomes

$$\dot{n}_1 = -\frac{1}{\Delta x} \frac{v_T x}{2} (n_1 - n_2 + n_{\text{ave}} q \frac{E \Delta x}{kT}). \quad (\text{A-8})$$

Comparing Eq. A-8 to the continuity equation ($\dot{n} = -\nabla \cdot J$), one can define an effective current density crossing the boundary between mesh points 1 and 2 as

$$J_{\text{eff}} = \frac{v_T x}{2} (n_1 - n_2 + n_{\text{ave}} \frac{qE \Delta x}{kT}). \quad (\text{A-9})$$

There is a conceptual difficulty with this effective current density if one lets the mesh width Δx approach zero. In that case, J_{eff} also approaches zero (for a smoothly varying density). However, the important point to remember is that J_{eff} is used in the code only in a form equivalent to Eq. A-8, which is independent of the mesh width, as it should be, for a smoothly varying density and an approximately constant E (that is, $\Delta x \ll$ a Debye length).

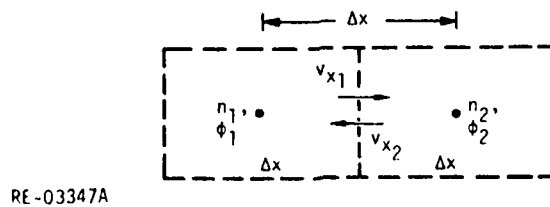


Figure 24. Two-mesh zone problem

It will be noted that Eq. A-9 has the same form as the current equations for electrons and holes in semiconductor theory if $v_T x \Delta x/2(kT/q)$ is identified as an effective mobility.

This similarity in the equations allows use of many of the analytical and computational techniques that have been developed to study semiconductor problems (Ref. 21). However, it is emphasized that this similarity is purely formal, and it is not implied that the repelled plasma has an actual mobility nor that this formulation is valid only in a very high-density plasma. The above derivation is dependent only on the assumption of quasi-equilibrium for the repelled species at every point in space.

A.3.2 Current Equation for Attracted Species

In the literature, it is generally assumed that the plasma species that is attracted to the probe experiences a "free-fall" acceleration toward the probe; that is, the kinetic energy of a particle at a position where the electrostatic potential is $\phi(x)$ is given by

$$\frac{m}{2} v^2(x) = \frac{1}{2} m v_i^2 + q \phi(x) , \quad (\text{A-10})$$

where v_i is the initial velocity of the particle in the region where $\phi(x) = 0$ (Ref. 5).

For an initial Maxwellian distribution of particles with a velocity distribution in the x direction given by

$$\frac{\partial(n/n_0)}{\partial v_{x_0}} = \left(\frac{m}{2\pi kT}\right)^{1/2} \exp(-mv_{x_0}^2/2kT) \quad (\text{A-11})$$

when the electrostatic potential is zero, the average velocity of all the particles that end up moving in the direction of the acceleration, when the local ϕ is non-zero, is given by

$$\begin{aligned} \overline{v_{x_+}} = & \int_0^{\infty} \sqrt{v_{x_0}^2 + 2q\phi/m} \frac{\partial(n/n_0)}{\partial v_{x_0}} dv_{x_0} \\ & + \int_{-\sqrt{2q\phi/m}}^0 \sqrt{2q\phi/m - v_{x_0}^2} \frac{\partial(n/n_0)}{\partial v_{x_0}} dv_{x_0} . \end{aligned} \quad (\text{A-12})$$

The first term in Eq. A-12 comes from the particles (half the total initial distribution) that have their initial v_{x_0} 's in the same direction as their final v_x 's. The second term comes from particles whose initial v_{x_0} 's were opposite in direction to the final v_x 's but were reversed by the accelerating fields.

Similarly, the average velocity of the particles whose initial v_{x_0} 's were opposite to the accelerating force but whose x velocities were never reversed in direction is given by

$$\bar{v}_{x-} = - \int_{-\infty}^{\sqrt{2e\phi/m}} \sqrt{v_{x0}^2 - 2e\phi/m} \frac{\partial(n/n_0)}{\partial v_{x0}} dv_{x0} . \quad (A-13)$$

When $\phi = 0$,

$$\bar{v}_{x+} = \frac{v_{Tx}}{2} = \sqrt{\frac{kT}{2\pi m}}$$

from Eq. A-4. The normalization density in Eqs. A-12 and A-13 is the total density n_0 . Thus, the flux moving in either the positive or negative direction with $\phi = 0$ is again $(n_0/2) v_{Tx}$, as discussed in Section A.3.1. When ϕ is not zero, the flux in the direction of the accelerating force is $n_0 \bar{v}_{x+}$, and in the direction opposite to the accelerating force is $n_0 \bar{v}_{x-}$.

Equations A-12 and A-13 can be put into the form

$$\frac{\bar{v}_{x+/-}}{v_{Tx}} = \int_{+/-}^{\infty} (B, v_{x0}) dv_{x0} , \quad (A-14)$$

where

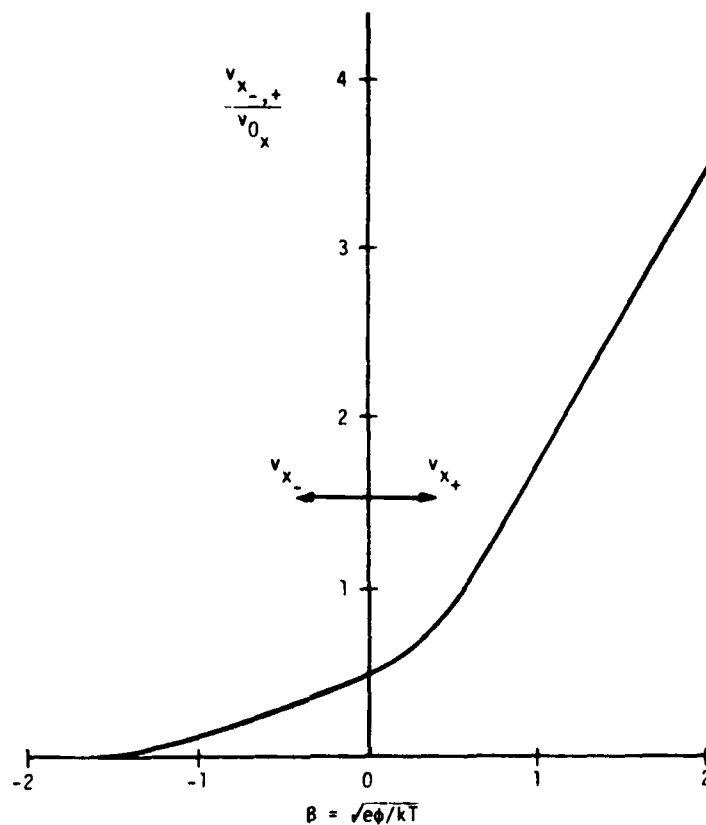
$$B = \sqrt{q\phi/kT} .$$

These equations can be numerically integrated very simply for various fixed values of B . The ratios $\bar{v}_{x+/-}/v_{Tx}$ are plotted vs. B in Figure 25. In the code, these functions are approximated numerically to give the flux of the attracted particles out of each mesh node (with potential ϕ) in the direction of the accelerating force (\bar{v}_{x+}) and opposite the accelerating force (\bar{v}_{x-}).

It is interesting that \bar{v}_{x+} can be approximated fairly well by

$$\frac{v_{Tx}}{2} \sqrt{1 + 4\pi q\phi/kT} .$$

In the limit of large ϕ , this velocity approaches $\sqrt{2q\phi/m}$; that is, all the particles are moving with the velocity corresponding to a kinetic energy equal to the potential energy, ϕ . Conversely, at large values of ϕ , \bar{v}_{x-} approaches zero, which means that there is no flux of particles opposing the accelerating force.



RE-03348

Figure 25. Average particle velocities as function of local potential, ϕ

A.3.3 Plasma Boundary Conditions at Inner Body and Outer Conductor

For the repelled species, the flux of particles into the inner body (that is, up to the body surface, where they are assumed to be captured or neutralized) is taken to be $\eta_B/2 v_{Tx}$, where η_B is the total density of particles just outside the body (Ref. 5) and v_{Tx} is the average thermal velocity in the x direction of half the particles η_B (Eq. A-4). This boundary condition is consistent with the assumption that the repelled species is everywhere in quasi-equilibrium; that is, half of the particles are moving toward the inner body and half are moving away, even adjacent to the body. In reality, right at the surface, there can be no outward current due to shadowing by the body (in the absence of secondary emission, which has been ignored thus far in this code).

However, to be consistent with the analytical treatments (Refs. 5,10) and the quasi-equilibrium assumption for the repelled particles, shadowing by the body is ignored.

At the outer boundary, the density of the repelled species is assumed to be fixed at the bulk value, n_0 . The net flux of these particles across the outer boundary is determined by Eq. A-9, where n_2 is the bulk density at the outer boundary, n_1 is the density at the first mesh point inside the boundary, and E is the electric field between these two points. The magnitude of this current is determined self-consistently in the code to satisfy the time-dependent rates of change of density inside the volume and the current of this species into the center body.

For the attracted species the flux into the center body is given by $n_B \bar{v}_{x+}$, where n_B is now the total density of the attracted species adjacent to the center body. Again, everywhere outside the center body, including the immediately adjacent mesh positions, it is assumed in the code that there is a flux of particles away from the center body given by $n_B \bar{v}_{x-}$. Very close to the center body, this outward flux should be reduced by shadowing. However, this shadowing effect has been ignored in the code. Fortunately, for large attracting potentials, \bar{v}_{x-} approaches zero, so the shadowing effect is correctly accounted for at large attracting potentials.

At the outer boundary, the density of the attracted species is also fixed at the value of the bulk density, n_0 . Thus, since the potential of the outer boundary is taken to be zero, there is an inward flux of attracted particles $(n_0/2)v_{Tx}$. However, there is also an outward flux of attracted particles from the first mesh point inside the outer boundary, given by $n_1 \bar{v}_{x-}$, where n_1 is the total density of attracted particles at the first zone inside the boundary. Thus, again, the net flux of the attracted particles across the outer boundary is determined self-consistently by the code to satisfy the time rate of change of the particle densities in the volume and the current into the center body.

A.3.4 Simulation of Emission Current

At present, the code cannot simulate the emission of a discrete beam of charge particles with finite initial energies. The simulation of emission current that is now in the code is equivalent to the outward emission of very high-energy particles, approximately uniformly from the surface area of the emitting body. The high-energy condition means that the emitted particles are slowed down negligibly by the body potential and their transit time from the emitting body to the outer boundary of the simulation volume (essentially a few Debye lengths away) is negligible compared to the response times of the

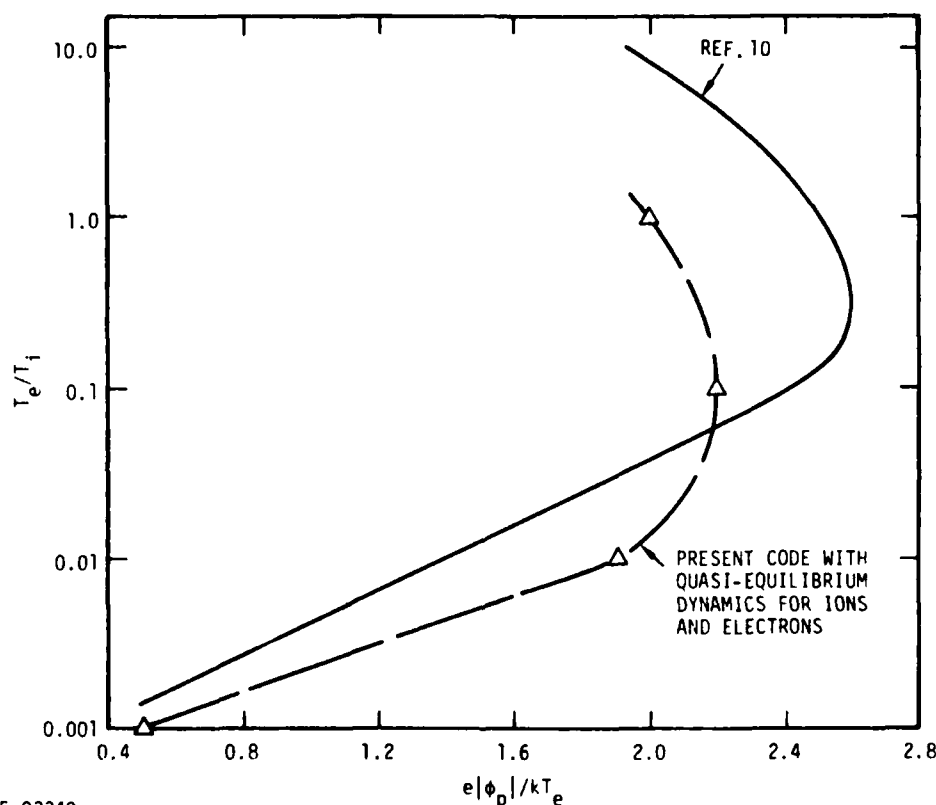
plasma. This condition means that the present code cannot simulate the nonlinear effects where the body potential would approach the beam energy and significantly slow down the beam particles.

The following is the procedure used in the code. At the start of a plasma problem, the Poisson-solver portion of the code is run first for a unit charge differential between the emitting body and the outer boundary. The code iterates the electrical fields until $\nabla \times E$ due to this charge differential is essentially zero throughout the volume, and then stores these normalized fields for future use. In the plasma problem, the amount of charge ΔQ that is emitted during each time step is assumed to instantly arrive at the outer boundary and instantly distribute itself over the outer boundary, consistent with a quasi-static charge differential. The electric fields at every point inside the simulation volume are then incremented by the normalized precharge fields calculated at the beginning of the plasma problem times the charge ΔQ emitted during that time step. The total resulting electric fields (the previous fields plus the increments due to ΔQ) then act on the two plasma species during that time step.

A.4 CODE STATUS AND PRELIMINARY RESULTS

As mentioned in Section A.1, an early version of this code, which treated both charge species in a quasi-equilibrium approximation, was used to try to reproduce the curve in Reference 10 for the potential of a non-emitting probe in a plasma as a function of the ratio of the electron and ion temperatures. In Figure 26, the present calculations are compared to the analytical result from Reference 10. Although the agreement between the two results is outside the bounds that one might expect just due to numerical computational techniques, the agreement is good enough to indicate considerable promise for the code, especially since the two models do not use precisely the same physics for the attracted species, and one geometry is cylindrical and the other spherically symmetric. Also, it should be pointed out that at least part of the discrepancy at the larger values of T_e/T_i results from these calculations being terminated before the slow-moving ions (small T_i) had reached a complete steady-state condition. In this early version of the code, explicit time integrations (using the velocities at the beginning of the time steps) were used to move the electrons and ions during the time steps. When the electron and ion velocities are widely different, as is the case with large T_e/T_i , computational instabilities in the electron densities usually result if the time step is made larger than the electron plasma period to speed up the calculations for the slowly responding ions. Difficulties

such as these can be overcome with implicit integration techniques that calculate the change in carrier densities during a time step, using some average velocity during that time step. This type of integration would be implemented in any future version of the code.



RE-03349

Figure 26. Comparison of present code with analytical predictions from Reference 10 (no secondary emission from probe). T_e and T_i are temperatures of electrons and ions, respectively.

The present status of the code is that the free-fall approximation for the attracted species has been programmed in a particular manner and a crude form of implicit integration has been implemented. However, there are some computational and physics difficulties with this formulation that require some additional work. It is anticipated that a more stable implicit integration procedure and the required new physics formulation could be accomplished with a modest effort.

A.5 FUTURE CODE CAPABILITIES

There are some additional problems for which a code such as the present one would be useful, but they would require some additional modifications to the present coding. Two of the more important applications are avalanche ionization of the neutral background gas by energetic electrons, either those emitted from the probe or those returning, and the effects of photo-ionization and the resulting photon-driven current when a photon beam interacts with the background neutral gas.

In both these problems, the question is how to combine the newly created electrons and ions, which would have some velocity distributions, with the already existing electron and ion densities, which would normally have different distributions.

A simple, but crude, approach would be to assume that the newly created particles have the same velocity distributions as the previously existing particles at every location in space. This approach might not be too erroneous for avalanche ionization, where the dominant velocities for the new and old electrons would at least be pointing in the same directions. However, it would be very poor for trying to simulate a photon-driven current at some angle to the dominant velocities.

A somewhat more refined approach would be to combine the momenta of the new and old particles vectorially at each mesh location and use the combined momentum (magnitude and direction) to specify the velocity of the shifted Maxwellian. Obviously, this approach is not vigorously correct either. However, Crevier (Ref. 22) has shown that a similar procedure, when used with SGEMP electrons, gave results that agreed very well with equivalent particle-pushing techniques. Apparently the details of the distributions are not too critical, at least for gross effects, as long as the momentum and energy of the plasma clouds are conserved. However, adoption of this approach would require a modification of the free-fall formalism, since the free-fall approach assumes that the net velocity of the plasma cloud is a function only of the local potential. A form of the free-fall coding which has been developed recently would be compatible with this approach for including electron and photon ionization. In addition, it appears that the new coding method will be computationally more stable. Again, these modifications to the code should not require an extensive effort.

REFERENCES

1. R. E. Leadon, J. V. Guillory, and N. A. Krall, "Review of Computer Codes and Experimental and Theoretical Literature for Possible Applications to Spacecraft/Particle-Beam/Plasma Problems," JAYCOR report 200-79-185/2172, prepared for ESD Hanscom AFB, 30 October 1979.
2. H. Cohen, private communication to H. Linnerud, March 1980.
3. S. H. Lam, "Unified Theory of the Langmuir Probe in a Collisionless Plasma," The Physics of Fluids, Vol. 8, No. 1, January 1965, p. 73.
4. L. W. Parker, "Plasmasheath-Photosheath Theory for Large High-Voltage Space Structures," Space Systems and Their Interactions with Earth's Space Environment, H. B. Garrett and C. P. Pike, ed., AIAA Progress in Astronautics and Aeronautics, Vol. 71, New York (1980), 477
5. F. J. Chen, "Electric Probes," form Plasma Diagnostic Techniques, ed. R. H. Huddleston and S. L. Leonard, Academic Press (1965), 113.
6. L. W. Parker and B. L. Murphy, "Potential Buildup on an Electron-Emitting Ionospheric Satellite," JGR, Vol. 72, March 1967, 1631.
7. J. E. McCoy, A. Konradi, and O. K. Garriott, "Current Leakage for Low-Altitude Satellites," Space Systems and Their Interactions with Earth's Space Environment, H. B. Garrett and C. P. Pike, ed., AIAA Progress in Astronautics and Aeronautics, Vol. 71; New York (1980), 523
8. R. R. O'Neil et al., "Summarized Results of the Artificial Aurora Experiment PRECEDE," JGR, Vol. 83, No. A7, July 1978, 3273.
9. A. J. Woods and T. N. Delmer, "The Arbitrary Body of Revolution Code (ABORC) for SGEMP/IEMP," DNA 4348T, 1 July 1976.
10. P. Rothwell et al., "Simulation of the Plasma Sheath Surrounding a Charged Spacecraft," AFGL report pres. at American Geophysical Union, June 1975.
11. L. G. Jacchia, "Thermospheric Temperature, Density, and Composition: New Models," Harvard Smithsonian Center for Astrophysical Research special report 375 (1977).
12. Satellite Environment Handbook, F. S. Johnson, ed., Stanford University Press (1965).
13. R. L. Arnoldy and J. R. Winckler, "The Hot Plasma Environment and Floating Potentials of an Electron Beam-Emitting Rocket in the Ionosphere," University of New Hampshire report, June 1978.

14. T. J. Hallinan, H. C. Stenback-Nielsen, and J. R. Winckler, "The Echo-4 Electron Beam Experiment: . . .," JGR, July 1, 1978 (3263).
15. H. A. Cohen et al., "Spacecraft Charging Due to Positive Ion Emission: An Experimental Study," Geophysical Research Letters, Vol. 6, June 1979, 515.
16. A. B. Langdon, "Kinetic Theory for Fluctuations and Noise in Computer Simulation of a Plasma," Phys. Fluids 22(1), January 1979 (163).
17. A. J. Woods et al., "Calculations of Charged-Particle Beam Emissions into A Neutral Plasma," JAYCOR report 200-79-182/2172, November 1979.
18. N. A. Krall and A. Trivelpiece, Principles of Plasma Physics, McGraw-Hill, New York (1973).
19. P. M. Banks and G. Kockarts, Aeronomy, Academic Press (1973).
20. R. Gendrin, "The French-Soviet 'ARAKS' Experiment," Space Sci. Rev. 15, 905 (1974).
21. R. E. Leadon and M. L. Vaughn, "Short-Pulsed Radiation Effects on Dynamic Electronic Components," DASA 2358, June 1969.
22. W. F. Crevier and D. W. Holst, "A Modified Fluid Approach to SGEMP and IEMP," pres. 1980 IEEE Conf. on Nuclear and Space Radiation Effects, Ithaca, New York, 15-18 July 1980.

